Influences of ~~iron and~~ manganese cycling on alkalinity in the redox stratified water column of Chesapeake Bay

Aubin Thibault de Chanvalon[1,2], George W. Luther[2], Emily R. Estes[2], Jennifer Necker[2], Bradley M. Tebo[3], Jianzhong Su[4,5], Wei-Jun Cai[4]

[1]Université de Pau et des Pays de l'Adour, E2S UPPA, CNRS, IPREM, Pau, France.
[2]School of Marine Science and Policy, University of Delaware, Lewes, Delaware, 19958 USA
[3]Division of Environmental and Biomolecular Systems, 3181 SW Sam Jackson Park Road, Portland, OR 97239, USA; Current address: Department of Chemistry, University of Washington, Seattle,WA 98195-1700
[4]School of Marine Science and Policy, University of Delaware, Newark, Delaware, 19716 USA
[5]State Key Laboratory of Marine Resources Utilization in South China Sea, Hainan University, Haikou, China

Correspondence to: A. Thibault de Chanvalon (aubin.thibault-de-chanvalon@univ-pau.fr)

Abstract. The ~~coastal~~ alkalinity ~~cycle~~dynamic in coastal environments controls the global burial of carbonate ~~which~~and modulates the ability of the ocean to trap anthropogenic CO_2. ~~Twelve~~Eleven high vertical resolution profiles from the temperate Chesapeake Bay estuary during two summers allow precise description of carbonate dynamics over the salinity and redox gradient along with the measurement of the speciation of most redox sensitive elements. In the presence of oxygen, carbonate dissolution, primary production and aerobic respiration are able to explain the evolution of total alkalinity (TA) versus dissolved inorganic carbon (DIC), once corrected for fresh and oceanic water mixing. A significant flooding event in 2018 ~~prevented the trapping of atmospheric CO_2 in the estuary and~~ favoured carbonate dissolution ~~to balance DIC consumption from photosynthesis.~~. In oxygen depleted waters, ~~a particularly high ratio~~2.4 mole of DIC is produced per 1 mole of ~~alkalinity versus~~TA production. This substantial DIC ~~occurred ($\Delta TA_{ex}/\Delta DIC_{ex} = 2.4$), that~~increase relative to TA has not been previously reported in the literature, and ~~that seemed invariant~~is consistent over the two years. The ~~stoichiometric analysis agrees with Mn measurements to explain~~stoichiometry of TA and DIC changes suggests this characteristic carbonate signature ~~by the critical role of~~is produced by MnO_2 reduction followed by Mn carbonate precipitation~~.~~ while direct observation highlights important Mn recycling in the water column. Our results underline that ~~Fe and~~ Mn ~~are~~is a critical ~~elements~~element of the alkalinity ~~cycle~~dynamic in the river dominated environment, especially ~~due to their~~because of its ability to limit the H_2S oxidation ~~into~~to SO_4^{2-} and by favouring sulphur burial.

1

1 Introduction

About ~~a third~~30% of anthropogenic CO_2 emission is rapidly trapped by dissolution in the ocean as dissolved inorganic carbon (DIC) which is dominated by bicarbonate ions (HCO_3^-, Friedlingstein et al., 2019). At the century time scale, atmosphere-ocean exchanges result in oceanic HCO_3^- enrichment not associated with a ~~Ca^{2+}~~cationic enrichment, in contrast to ~~the HCO_3^- released from continental erosion~~silicate or carbonate weathering (preponderant at thousands to a million year scale, Urey, 1952). This disequilibrium corresponds to an excess of proton release compared to carbonate ions during CO_2 dissolution that is only balanced in the deep ocean by increasing Ca^{2+} production from carbonate dissolution, a process named the chemical carbonate compensation (Boudreau et al., 2018). However, in most shallow ~~water~~waters, where carbonate precipitation largely predominates over dissolution and accounts for 2/3 of buried carbonate (Smith and Mackenzie, 2016), other, localised processes may constrain the carbonate dynamic (Borges et al., 2006; Lohrenz et al., 2010). For example, some calcifying species may slow down their carbonate precipitation in case of pH decrease (so called biological carbonate compensation; Boudreau et al., 2018). As another example, in estuaries, the seasonality of river flow, temperature and continental erosion modulate $CaCO_3$ dissolution (e.g. Su et al., 2020b), atmospheric CO_2 exchanges (e.g. Borges et al., 2018) or respiratory activity ~~(Abril et al., 2003)~~(e.g. Abril et al., 2003). As recently highlighted (Middelburg et al., 2020), the transfer of carbonate particles over estuaries is poorly estimated due to a sparse dataset (Meybeck, 1987).

In anaerobic environments, sulphate consumption increases the observed alkalinity mainly due to the "charge transfer" from SO_4^{2-} to HCO_3^- (Hu and Cai, 2011). Although correct, this approach tends to neglect the roles of Fe and Mn oxides (Middelburg et al., 2020) since their transformation from (oxyhydr)oxides into sulphur or carbonate species does not change the charge they bear. However, metal oxides are critical since they are the main H_2S oxidation pathway that does not regenerate SO_4^{2-} but rather produces S^0 instead (Findlay et al., 2014; Avetisyan et al., 2021). Their contribution depends on the solid phases buried in the sediment, but should also be revealed by the specific changes of alkalinity and inorganic carbon they produce.

To better constrain the carbonate cycle in temperate microtidal estuaries ~~and the associated HCO_3^- dynamics~~, we sampled a stratified water column in the Chesapeake Bay ~~a dozen~~eleven times over two campaigns with a high vertical resolution (down to 10 cm). This protocol allows a precise description of carbonate dynamics over a redox gradient along with the measurement of the speciation of most redox sensitive elements. Such sampling ~~can thus illustrate~~illustrates carbonate chemistry on transitioning from oxygenated waters to waters devoid of oxygen as usually only encountered in sediments or in anoxic lakes or seas (*e.g.* Black Sea). The original observed changes of alkalinity versus ~~DIC~~dissolved inorganic carbon changes are interpreted based on ~~anoxic~~typical geochemical reactions occurring along the redox gradient.

2

2 Materials and methods

2.1 Sampling

During two sampling ~~campaign~~campaigns from August 3rd to 9th, 2017 and July 28th to August 3rd 2018, eleven profile casts were conducted in a ~~25 m water depth~~ unique station in the Chesapeake Bay with a water depth of 25 m (Station 858, 38°58.54'N; 076°22.22'W). The Susquehanna River is the main tributary of the bay representing on average 2/3 of the fresh water input (Zhang et al., 2015). Despite similar season, the two campaigns occurred at very different river flow with about 850 m^3 s^{-1} in 2017 versus 8500 m^3 s^{-1} in 2018 due to release of flood waters from the Conowingo Dam ~~and which.~~ The August 2018 condition corresponds to flooding which occurs on average every 3.5 years (return period of 3.5 years ~~,~~. USGS survey).

Each CTD cast was performed during low or high tide slack periods. An oxygen sensor (Clark electrode, SBE Inc.; detection limit of 1 μM) and fluorescence sensor (Eco-FL Fluorometer, WETLabs) were part of the CTD Rosette to take measurements during sampling. Also, a submersible all plastic pump profiler was attached with the pump near the sensor orifices allowing measurement and sampling at a resolution of a few centimetres over 25 m water depth. Water was pumped to the deck within 1 minute and water passed through a flow through voltammetry system measuring continuously O_2, Mn(II), Fe(II), organically complexed Fe(III), FeS clusters, H_2S and polysulfides (Hudson et al., 2019). When redox interfaces were identified, samples were filtered through an acetate cartridge filter (pore size 0.45 μm) for pH and inorganic carbon parameters, which were processed onboard within a few hours after sampling in order to conserve chemical speciation. The pump profiler system was cleaned with ~~DI~~deionised water (18 MΩ) onboard the deck of the ship after deployment. No coating effects were observed with the pump system.

2.2 Discrete Measurements

For each sample, all redox species were determined in the through flow voltammetry system using cyclic voltammetry with a 100 μm diameter Au/ Hg amalgam PEEK microelectrode prepared according to Luther et al. (2008) connected to a DLK-60 electrochemical analyser from Analytical Instrument Systems Inc. The detection limit of this method is 0.2 μM for sulfide and polysulfides. Discrete samples for the determination of NO_2^-, Fe and Mn species were filtered through nylon luer-lock syringe filters (Millipore, 0.20 μm~~) filters.~~). Iron was measured based on the ferrozine method (Stookey, 1970): after HCl acidification and an optional reduction step with hydroxylamine hydrochloric (final concentration 0.7 M) for 1 hour, ammonium actetate (final concentration 0.5 M) and ferrozine (final concentration 1 mM) were added and absorbance at 562 nm was read with a diode array spectrophotometer (Hewlett Packard 8452B). Limit of detection is 100 nM for Fe(II). Shipboard nitrite determination was performed using the method of Grasshoff (1983). To 25 ml of sample, 0.5 ml of ~~58mM~~58 mM sulfanilamide in 10% v/v HCl and 0.5 ml of a ~~4mM~~4 mM N(1-naphthyl)ethylene diamine hydrochloride solution were added. Samples with added reagents were shaken and left to sit for 15 min, followed by UV–Vis analysis at 540 nm using a 10-cm cell to increase detection limits. Calibration curves were constructed using sodium nitrite. Limit of detection is 10 nM for NO_2^-.

3

Dissolved manganese was determined by displacement of a Cd(II)-porphyrin complex with Mn(II) to form the Mn(II)-porphyrin complex (Ishii et al., 1982). Mn(III) species were identified based on slower reactivity with the Cd complex (Madison et al., 2011) as modified in Thibault de Chanvalon and Luther (2019). Alternatively, Mn(III) species were identified after HCl treatment (down to pH=1.5) ~~follow~~followed by filtration in order to flocculate and eliminate the dissolved manganese bound to humic material by filtration (Oldham et al., 2017b). Limit of detection is 50 nM for Mn(II). MnOx was measured on 20 mL samples of suspended material retained on 0.2 µm filters by the Leucoberbelin blue (LBB) method (Jones et al., 2019). Four millilitres of a reagent solution ([LBB]= 78 µM, [acetic acid]=14mM) react with the filter and the absorbance is read at 624 nm. $KMnO_4$ was used to calibrate the LBB method which allows the calculation of the electron equivalents obtained from particulate MnOx. Results are given in as MnO_2 equivalent with a limit of detection of 0.1 µM and an uncertainty below 5%.

The DIC samples were preserved in 250-mL borosilicate glass bottle with 50 µL saturated $HgCl_2$ solution. The total alkalinity (TA) samples were not poisoned to prevent HgS precipitation and H^+ release in anoxic and low salinity waters (Cai et al. 2017). ~~The DIC samples were measured by a nondispersive infrared analyzer (AS-C3, Apollo Scitech) within a week (Huang et al. 2012). The total alkalinity (TA)~~ Then TA was ~~analyzed~~analysed by Gran titration in an open-cell setting (AS-ALK2, Apollo Scitech) ~~inboard~~ within 24 h of collection (Cai et al. 2010a). The DIC samples were measured by a nondispersive infrared analyzer (AS-C3, Apollo Scitech) within a week (Huang et al., 2012). The precision for DIC and TA was about 0.1%. Both DIC and TA measurements were calibrated against certified reference materials~~.~~ (CRMs Batch 163 and Batch 173 provided by Andrew Dickson of the Scripps Institution of Oceanography). The pH samples were measured onboard at 25 ° C within 1 h of collection using an Orion Ross glass electrode, and calibrated with NIST standard buffers. The pCO_2, calcite saturation and TA were calculated from measured DIC and ~~TA~~pH via ~~an excel sheet implemented with values from (Millero, 1995) and further validated using~~ CO2sys program~~.~~ using Cai and Wang (1998) constants. The measured TA was found highly correlated to ~~TA~~the calculated ~~with CO2sys using pH and DIC as input value~~TA (r^2 = 0.~~995 and 0.~~998, slope = ~~1.03) suggesting~~0.995 and 1.017 for 2017 and 2018 campaign respectively) and their difference was always below 30 µM with an average of 7.5 µM for 2017 and of 22.2 µM in 2018. These results suggest low ~~effect of~~contribution of non-carbonate species (e.g. nitrite, ammonium or organic ~~alkalinity~~matter (Cotovicz Jr. et al., 2016)~~.~~) and measured TA was used for the interpretation.

2.3 Models of biogeochemical process on TA and DIC

2.3.1 ~~Observed changes induced by biogeochemical process~~

~~To distinguish TA and DIC changes produced by~~ Identification of biogeochemical processes from ~~scatter plots: the river/ocean mixing~~hammer, ~~the excess of TA and DIC, noted TAex and DICex have to be calculated. This excess corresponds to the cumulative effects from all unknown biogeochemical processes observed.~~ bow and the spear

As total concentrations, TA and DIC are conservative during mixing ~~and can be easily calculated as~~ which means that they ~~obey to~~ the deviation from the river-ocean mixing line after identification of riverine and oceanic endmembers. In contrast, pH and ~~law:~~

4

$$C = C_A \chi + C_B (1 - \chi) \tag{1}$$

With C_A and C_B the concentration at the two endmember locations A and B; C is the concentration of the mixture and χ is the contribution of endmember A relatively to the contribution of endmember B. In case of two water masses at the locations A and B, respectively, any pairs of elements conservative by mixing whose concentrations ~~of individual C species are not conservative. The oceanic endmember selected in this study~~ C and D can be defined by the endmember C_A, D_A at the location A and C_B, D_B at the location B obeys the equation 2:

$$C = C_B - D_B \frac{C_A - C_B}{D_A - D_B} + D \frac{C_A - C_B}{D_A - D_B} \tag{2}$$

Equation (2) demonstrates that mixing of two conservative elements between two endmembers results in a straight line passing through the points of coordinates $(C_A;D_A)$ and $(C_B;D_B)$. This "endmember driven" interpretation is illustrated in Fig. 1a and stands on the implicit assumption that the endmembers are stable over time– they should be hammer-fixed nails. In an environment where at least one of the endmembers changes too fast, equation 2 is not as valuable. Endmember changes can occur due to processes external to the system studied, such as a river endmember varying according to weathering inputs and biogeochemical reactions in rivers and drainage basins (Officer, 1979; Boyle et al., 1974).
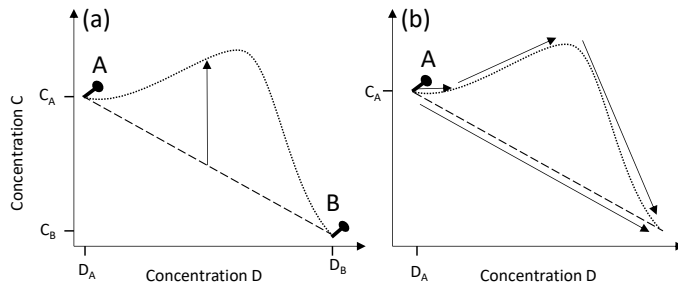

Figure 1: Theoretical scatter plot of two species (dashed and dotted line) conservative by mixing. A) two possible "endmember driven" interpretations. B) two "reaction driven" interpretations. A segment, as represented by the dashed line, can be interpreted as a conservative mixing between two endmembers as described in A), the hammer-fixed nails interpretation, or as the result of a geochemical signature as indicated by the arrow in B), the spear interpretation. A curve, as represented by the dotted line, can be interpreted as an excess (from biogeochemical process or additional source) superimposed to a mixing as described by the arrow in A), the bow interpretation, or as a succession of multiple geochemical reaction as described by the arrows in B), the spears interpretation.

In the case of an estuary with stable endmembers and without significant lateral effluents, any deviation from the mixing line signals the occurrence of one or more biogeochemical processes easily identified in a scatter plot; the bow interpretation (the arrow between the dashed and the dotted line in Figure 1A). Due to the different rate of mixing and rate of reaction and because these variables are not separated in the differential equation describing this behaviour, mathematics alone does not help further in the interpretation. However, the difference between the observation and the mixing prediction is indicative of

5

the non-conservation production or removal of the element(s) being studied. In our case, this deviation is measured using the observed TA and DIC vs those predicted from their conservative behaviour based on salinity as described by equations 1 and 2. These deviations are usually called the excess of TA (or TAex) and the excess of DIC (or DICex). In our case, the oceanic endmember was the one proposed by Su et al. (2020a) for both ~~DIC and TA. However, the upstream estuary endmember from~~
~~Su et al. (2020a) corresponded to the Chesapeake Bay in 2016 with a river flow of only 226 m³ s⁻¹. The two~~ August campaigns ~~described here are characterised by much higher river flow. Since large~~. The oceanic endmember varies mainly with season (Cai et al., 2020) and a change of 50 µM results in 5% uncertainty on the slope of the mixing line. Large variations exist in the upstream estuary endmember mainly due to changes of weathering intensity and riverine discharge (Meybeck, 2003; Joesoef et al., 2017)~~, we slightly modify the TA~~ and a one-off endmember ~~of Su et al. (2020a)~~has to ~~improve the~~be determined by fit with the in situ measurements ~~with~~at the lowest measured salinity (Fig. A1). ~~Such changes were not necessary for DICex~~
~~calculation. This~~The upstream endmember is not a river endmember (Su et al., 2020a) but ~~correspond~~corresponds to a salinity above 1.5 preventing any interpretation for biological activity in the fresh water part of the estuary (Meybeck et al., 1988). ~~Compared~~However, it corresponds ~~to Su et al. (2020a),~~a larger water mass pool, less sensitive to short term changes and thus more likely to satisfy the condition of stability of the endmember.

In case of a water mass isolated from any exchange, including air-water exchanges, but submitted to a given reaction with C and D being the reactants, E and F the reaction products, and α_i being the stoichiometry of species (equation 3), the variation of the species C and D obeys equation 4, with v the rate of the reaction, which can be determined in equation 5.

$$\alpha_C C + \alpha_D D = \alpha_E E + \alpha_F F \qquad (3)$$

$$\frac{dC}{dt} = -\alpha_C\, v \ \text{ and } \ \frac{dD}{dt} = -\alpha_D\, v \qquad (4)$$

$$\frac{dC}{dD} = \frac{\alpha_C}{\alpha_D} \qquad (5)$$

Equation 5 indicates that the ratio of small variations over time of two species is equal to the ratio of the stoichiometry of the reactions governing their transformations, whatever the exact rate of the reaction is. In our case, in a plot representing TAex versus DICex, the local slope ~~change associated is mostly insignificant (TAex/DICex differs by less than 0.2) and~~
~~represents the~~ΔTAex/ΔDICex over time would be equal to the stoichiometry of the occurring reactions, which corresponds to the "reaction driven" interpretation or the spear interpretation as illustrated in Fig. 1B. The uncertainty of ~~our description. The~~ ΔTAex/ΔDICex is equal to the sum of the relative uncertainty of ΔTAex and ΔDICex. Posing ΔTA the change of TA measured, ΔS the change of salinity and sml_TA, the slope of the mixing line for TA, we have ΔTAex = ΔTA – sml_TA x ΔS. Uncertainty on ΔTA and ΔS are negligible to the relative uncertainty of slope_ml and posing δ(x) the uncertainty on x, we get:

$$\frac{\delta\,(\Delta TAex/\Delta DICex)}{\Delta TAex/\Delta DICex} = \frac{\delta(\Delta TAex)}{\Delta TAex} + \frac{\delta(\Delta DICex)}{\Delta DICex} = \frac{\delta(sml\_TA)}{sml\_TA} + \frac{\delta(sml\_DIC)}{sml\_DIC} = 0.1 \qquad (6)$$

6

However, if the temporal evolution of water masses is visible in space, it requires that some mixing occur which puts into question the validity of equation 5 defined for time variations alone. By the way, equation 6 describes the behaviour of a solute, conservative by mixing, in case of turbulent diffusion mixing (sometimes called eddy diffusion or diffusive like mixing) superimposed on a chemical reaction as described in equation 3, with D_s the effective diffusion coefficient:

$$\frac{dC}{dt} = -D_s \frac{d^2C}{dx^2} + \alpha_C \, v \qquad (7)$$

165   Assuming steady state, *i.e.* dC/dt=0, applying equation 7 to two different species sharing the same reactions at rate v, we can express the rate of the reaction as

$$-\frac{v}{D_s} = \frac{1}{\alpha_C}\frac{d^2C}{dx^2} = \frac{1}{\alpha_D}\frac{d^2D}{dx^2}$$

By integration with respect to x, it becomes equation 8:

$$\frac{dC}{dx} = \frac{\alpha_C}{\alpha_D}\frac{dD}{dx} + G \qquad (8)$$

      This is valuable at any position, with G being the constant rising from the integration. If, at the initial location, mixing is negligible then equation (5) is valuable, so G=0 and equation (8) is equivalent to equation (5), but particularly valuable in the

170 case of turbulent diffusion mixing at steady state.

      Therefore, away from atmospheric exchanges, in case of turbulent diffusion mixing and steady-state, TAex and DICex correspond to ~~an excess from~~ a sum of biogeochemical reactions spread all over the ~~estuary and~~water column that can ~~therefore~~be decomposed into several ~~components induced by~~reaction zones. In each zone, the local ΔTAex/ΔDICex ratio will equal the apparent stoichiometry of a combination of the biogeochemical reactions occurring in this zone. In case of multiple

175 ~~localised geochemical reactions, ΔTAex and ΔDICex~~simultaneous reactions in the same zone, by posing α_C^i the stoichiometry of the ith reaction concerning the reagent C and v^i the reaction rate of the ith reaction, we obtain:

$$\alpha_C v = \sum_i \alpha_C^i v^i$$

To maintain a global reaction rate independent to the species we have

$$v = \sum_i v^i$$

so
$$\alpha_C = \frac{1}{v}\sum_i \alpha_C^i v^i \qquad (9)$$

      Equation 9 indicates that the apparent stoichiometry in a given zone corresponds to the sum of the stoichiometric coefficients of each reaction weighted by the relative rate of each reaction. Therefore, to estimate the relative rate of each

7

180   reaction to the observed local changes of TAex, DICex and AOU or H$_2$S, a linear combination of reactions is calculated. This combination has to fit 3 equations (one for each parameter) which allows a maximum of 3 reactions to be used to solve the system. A limited number of reactions is selected as candidates based on the discussion (see Table 1 and sections 4.2 and 4.3). Then, the system is solved with the minimum possible reactions and the weighted coefficients, v^i/v, are calculated.

2.3.2 TA changes indicated by reactions' stoichiometry

185   ~~The simplest way to calculate the TA changes induced by individual, localised, geochemical reactions (ΔTAex) is to do a direct look to reaction stoichiometry. Indeed, it is possible to mathematically separate acid active and acid inactive species. Active species are defined as species forming acid-base couples whose one form is able to exchange protons during the titration of a sample down to pH 4.5 either as electron donor or as acceptor, such as NH$_3$ or HCO$_3^-$ while inactive species include Cl$^-$, SO$_4^{2-}$ and Ca^{2+} among others. Writing z, the charge held by a species, the electroneutrality of water can be written as Eq. (1).~~

190   The simplest way to calculate the TA changes induced by an individual reaction is to do a direct look to reaction stoichiometry. Indeed, the total alkalinity (TA) corresponds to the quantity of acid added to titrate a solution down to pH 4.5 (Dickson, 1981). It can be described by the equation (10), with the example of HCl as acid and B$^-$ any titrated base.

$$0 = \sum z_{\text{inactive}} + \sum z_{\text{active}} \quad HCl + B^- \rightarrow BH + Cl^- \tag{$\cancel{1}$10}$$

    ~~The total alkalinity (TA) corresponds to the quantity of acid added to titrate a solution down to pH 4.5 (Dickson, 1981), according to Eq. (2), with the example of HCl as acid and B$^-$ any titrated base.~~

$$\cancel{HCl + B^- \rightarrow BH + Cl^-} \tag{$\cancel{2}$}$$

195   Assuming a complete reaction, the quantity of acid added is equal to the negative charges initially present in the sample consumed ~~from~~plus the ~~active~~positive charges added to the species ~~pool (Cl$^-$ is inactive). Indeed, the titration transfers the charges from the acid active pool to the acid inactive pool~~initially present in the sample. Thus, the total alkalinity corresponds to the loss of negative charges (or gain of positive charges) for ~~active~~ species initially present in the sample produced by the pH change from the initial pH = pHini to pH = 4.5 ~~(Eq. (3)):~~. Writing z_i^{pH}, the charges held by any specie i, initially present

200 in the sample at a given pH, we get equation (11):

$$\cancel{TA = \sum z_{\text{active}}^{pH=4.5} - \sum z_{\text{active}}^{pHini}} \quad TA = \sum_i z_i^{pH=4.5} - \sum_i z_i^{pHini} \tag{$\cancel{3}$11}$$

    ~~Equation (1) can be reorganized and combined with Eq. (3) leading to Eq. (4) :~~

    However, the electroneutrality of water induces:

$$\cancel{\sum z_{\text{inactive}} = -\sum z_{\text{active}}^{pHini} + \sum z_{\text{active}}^{pH=4.5} - \sum z_{\text{active}}^{pH=4.5}} \quad \sum_i z_i^{pHini} = 0$$

8

$$\text{TA} = \sum z_{inactive} + \sum z_{active}^{pH=4.5} \text{TA} = \sum_i z_i^{pH=4.5}$$ (4 12)

From Eq. (4), one can easily deduce the changes of alkalinity. Most Equation (12) demonstrates than the total alkalinity is simply the sum of charges that each species present in the sample would have at pH 4.5. From Eq. (12), one can easily deduce the changes of alkalinity from any reaction stoichiometry as soon as the bearing charges at pH = 4.5 are known. For example, for a 0.0020 M NaOH solution, its TA is simply 0.0020 M as at pH=4.5, TA= ($[Na^+] + [H^+] - [OH^-]$) = 0.002 + $10^{-4.5}$ – $10^{-14+4.5}$ = 0.0020 M. For natural waters, most of the time, the only charged active species at pH = 4.5, are $H_2PO_4^-$ and NH_4^+. In that respect, whatever the initial pH and the acid-base equilibrium of species in the sample, the sum of phosphate species will count negatively and the sum of ammonium species will count positively. Strictly speaking, at pH=4.5, acid species with pKa between 2.5 and 6.5, such as F^- and NO_2^-, would be only partially titrated and the charge equals their concentration multiplied by a correction factor of $(1+10^{pKa-4.5})^{-1}$, but this correction can be neglected to a first approximation. The Eq. (4) corresponds (12) are equivalent to those published in Soetaert et al. (2007) or Wolf-Gladrow et al. (2007) whose equation 32 can be find back replacing the two term in Eq. (4) by:

$$\sum z_{inactive} = [Na^+] + 2 [Mg^{2+}] + 2 [Ca^{2+}] + [K^+] + 2[Sr^{2+}] + \cdots - [Cl^-] - [Br^-]$$
$$- [NO_3^-] - 2TSO4 - THF - THNO2 - \cdots$$

$$\sum z_{active}^{pH=4.5} = -TPO4 + TNH3$$

where TPO4 = $[H_3PO_4] + [H_2PO_4^-] + [HPO_4^{2-}] + [PO_4^{3-}]$, TNH3 = $[NH_3] + [NH_4^+]$, TSO4 = $[SO_4^{2-}] + [HSO_4^-]$, THF = $[F^-] + [HF]$, and THNO2 = $[NO_2^-] + [HNO_2]$. However, the Eq. (4) is. However, the Eq. (12) are more synthetic and more general. For example, in suboxic water, specific species such as polysulfides (as HS_8^{2-}, Rickard and Luther, 2007) and in highly productive environment environments, carboxylic group groups from DOC can be easily added as soon as the bearing charges at pH = 4.5 are known. Finally, note that the definition of active species used differs from the weak acid-base couple definition, since our definition classifies the weak acid –based couples with pKa between -1.75 and 4.5 as inactive species, but the reasoning would be similar if the term active/inactive species is changed by weak/strong acid-base couple.

2.3.3 Linear combinations of reactions

To estimate the participation of each reaction to the observed changes of TAex, DICex and AOU or H_2S, a linear combination of pre-selected reactions is calculated. This combination has to fit 3 equations (one for each parameter) which allows a maximum of 3 variables to be used to solve the system. Each reaction being one variable, a limited number of reactions is selected as candidates based on the discussion (see section 3.3.2). Then, the system is solved with the minimum possible reactions.

9

3 Results ~~and Discussion~~

3.1 Water column stratification

High-resolution ~~(< 1 m)~~ profiles of ~~carbonate~~salinity and temperature plotted in Fig. 2 shows the stratified water column at
230 station 858. Carbonate and redox chemistry are plotted against salinity in Fig. ~~1~~3. These data result from the 11 CTD casts
performed over 1 week during each campaign and correspond to depths ranging from ~~2~~0.7 to 25 meters. ~~While direct plots~~
depth. Plots against depth generate ~~noisy~~noisier profiles ~~that~~ are ~~less informative,~~shown in Appendix 2 while plots against
salinity ~~provide consistent information about~~follow the ~~processes~~water masses. Despite the overall ~~much~~ lower salinity due to
a near 7-fold river flow increase in 2018 than 2017 (5800 m s^{-1} in 2018 versus 850 m^3 s^{-1} in 2017), similar zonation of the
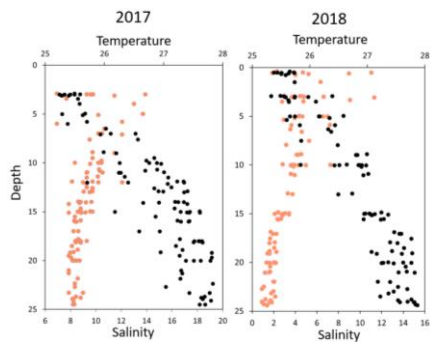
Figure 2: Superimposed salinity (in black) and temperature (in orange) profiles over the 11 casts for each campaign.

235 water column occurred.

A surface layer sampled only in 2018 is visible in the top 3 meter depth. It presents highly variable temperature and oxygen
concentration and oversaturation of pCO2 indicating export to the atmosphere. Below, at 3 meter depth, a subsurface layer
(named primary production zone or PP in Fig. ~~1~~3) is characterized by a high amount of O$_2$ (about or above 100% saturation),
high pH (~~above~~about 8; 8.11 ± 0.07, n=13 in 2017 and 7.~~5~~94 ± 0.08, n=14 in 2018), high day to day temperature variation
240 (above 1 °C between different days) and low pCO$_2$ (below atmospheric CO$_2$ of ~~400 µatm). This signature corresponds to~~
~~important atmospheric exchange and~~407 µatm (Chen et al., 2020); 505 ± 75 µatm, n=13 in 2017 and 770 ± 130 µatm, n=14
in 2018 with minimal value at 110 µatm in 2017 and 205 µatm in 2018). This signature corresponds to important primary
production (PP). Fluorescence (not shown) correlates with pH as expected for primary production (pH = Fluo (mV) x 13 +7.14,
r^2=0.8 in 2017 and r^2=0.9 in 2018). DICex and TAex reach their minimal value in this surface layer. While DICex minimum
245 is similar between the two campaigns (78 ± 17 µM, n= 13 in 2017 and 76 ± 10 µM, n=14 in 2018); TAex minimum is much
lower in 2017 (7 ± 3 µM, n=12) than in 2018 (48 ± 7 µM, n=14).

10

Below, with increasing ~~depth~~salinity, an important increase of pCO_2 accompanying the decrease of O_2, pH and temperature is visible. A relatively invariable low ~~O_2~~oxygen zone (called ILO in Fig. ~~1~~3) is here defined by the ~~depth~~salinity invariance of
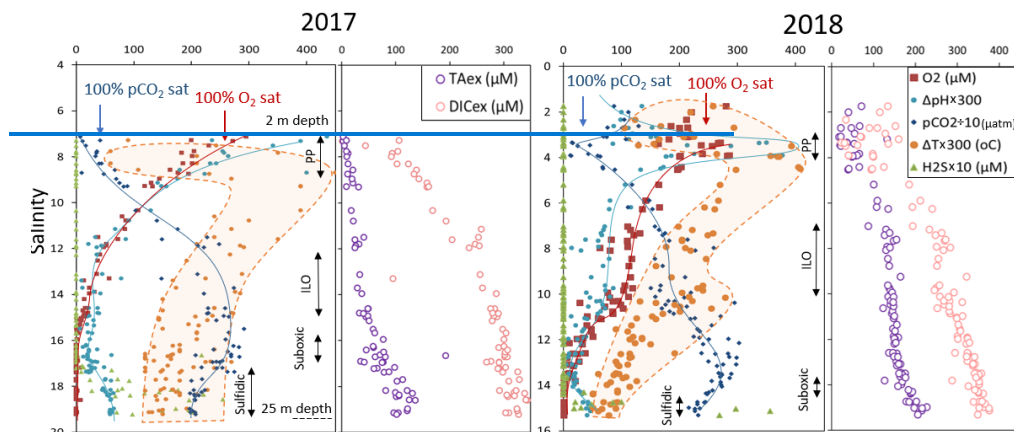
Figure 1: Superimposed carbonate and redox chemistry profiles over 11 casts. Simple mathematic transformation allows to plot all variable on the same scale, lines are only here to guide eyes. Base line for temperature is 25 °C and base line for pH 7.175. For example, pH maximum value of 400 correspond to a pH=400/300+7.175=8.5, a reading at 100 for pCO₂÷10 indicates a value of pCO₂ = 1000 µatm.

O_2 concentrations, ~~and corresponds to a concentration of~~ at about ~~30~~24 ± 3 µM, n=15 in 2017 and ~~110~~105 ± 5, n=16 µM in 2018. Other species are also relatively stable for this depth such as pCO_2, at about ~~2500~~3250 ± 150 µatm, n=10 in 2017 and ~~1800~~2590 ± 100 µatm, n = 16 in 2018, and pH, about 7.~~3~~28 ± 0.01, n=13 in 2017 and 7.~~4~~37 ± 0.02, n=16 in 2018. Deeper, where the oxygen is not detectable (< ~ 1 µM), the so-called suboxic zone corresponds to a pH minimum at 7.~~2~~24 ± 0.01, n=40, similar in 2017 and 2018 that generates a pCO_2 maximum. The deepest layer is a sulfidic layer ([H_2S] = 11.2 ± 2.8 µM n=36) in which the pH seems quite stable at 7.~~4~~33 ± 0.01, n=29 and 7.~~3~~32 ± 0.01, n=9 in 2017 and 2018 respectively. ~~The main changes between the two campaigns correspond to a greater oxygen penetration in 2018, preventing nitrite accumulation, and to the appearance of a surface layer (with salinity below 3) that stands above the primary production zone in 2018.~~

11

The Ca^{2+} concentrations observed by Su et al. (2021) and during the 2018 cruise (data not shown) vary linearly with salinity (calcium excess stay below 200 µM or 10% of total Ca). Assuming similar behaviour in 2017, calculations show that the whole water column (except 4 samples from the PP zone) is under saturated ($0.36 < \Omega cal < 1$; mean=0.68) with respect to calcite in 2018, while undersaturation is only valid below S=10 in 2017. The main changes between the two campaigns correspond to a greater oxygen penetration in 2018, especially visible in the ILO zone. Additionally, a surface layer (with salinity below 3) is visible above the primary production zone in 2018 but is related to the more superficial sampling in 2018.
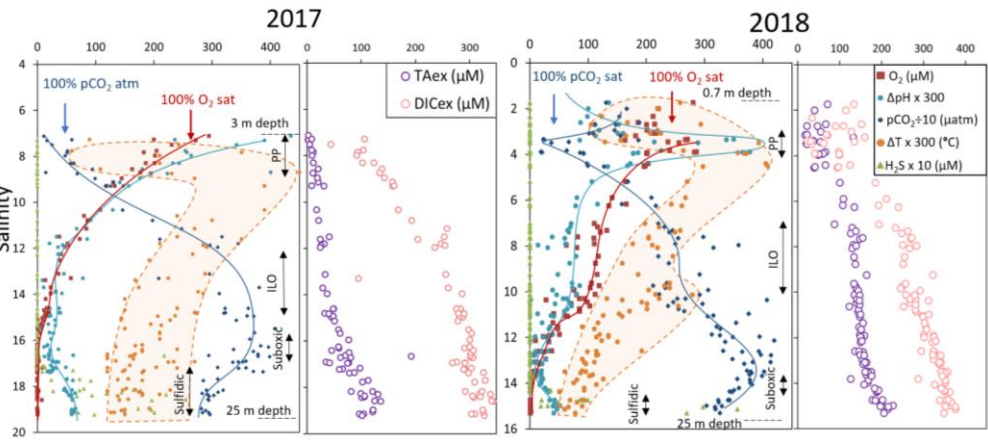
Figure 3: Superimposed carbonate and redox chemistry profiles of 11 casts done in august 2017 (left) and 11 casts done in august 2018 (right). Linear mathematic transformation allows to plot all variable on the same scale, lines are only here to guide eyes. In particular T = 25 + ΔT/300 and pH= 7.175 + ΔpH/300. For example, pH maximum value of 400 correspond to a pH=400/300+7.175=8.5, a reading at 100 for pCO$_2$÷10 indicates a value of pCO$_2$ = 1000 µatm.

12

3.2 Intermediate redox species

The development of the suboxic zone during summer (Su et al., 2021) and the regularity of this development over the years ~~(Sholkovitz et al., 1992; Trouwborst et al., 2006; Lewis et al., 2007; Cai et al., 2017; Oldham et al., 2017a)~~(Sholkovitz et al., 1992; Trouwborst et al., 2006; Lewis et al., 2007; Cai et al., 2017; Oldham et al., 2017a), requires the presence of species able to rapidly oxidise the H_2S mixing upward and to reduce the O_2 mixing downward. The three main redox couples known to play this role, NO_3^- / NO_2^-, MnO_x / Mn^{2+} and Fe^{3+} / Fe^{2+} are described in the Fig. ~~2~~4 by the superimposition of all cast results against salinity. Four representative casts are plotted in the Fig. ~~A2. NO_2^- reaches a maximum in the ILO zone, at low but measurable oxygen concentrations. Because of the presence of oxygen, the NO_2^- production would be more likely associated with nitrification of the NH_4^+ diffusing upward rather than denitrification despite the possibility of reducing conditions occurrence in micro niches. Just below oxygen depletion, in the suboxic zone, MnOx reaches a maximum probably produced by the Mn^{2+} diffusing upward that is biologically oxidized by very low, undetected, O_2 concentration (Clement et al., 2009). Additionally, Mn^{2+} could be oxidized by the nitrite diffusing downward (thermodynamically favourable (Luther, 2010)), it is also possible that the Mn oxidation is produced by chemodenitrification i.e. by reduction of (not measured) nitrate into nitrite. The MnOx decrease fits perfectly to the Mn^{2+} increases in sulfidic conditions (Fig. 2) according to the reduction of settling~~
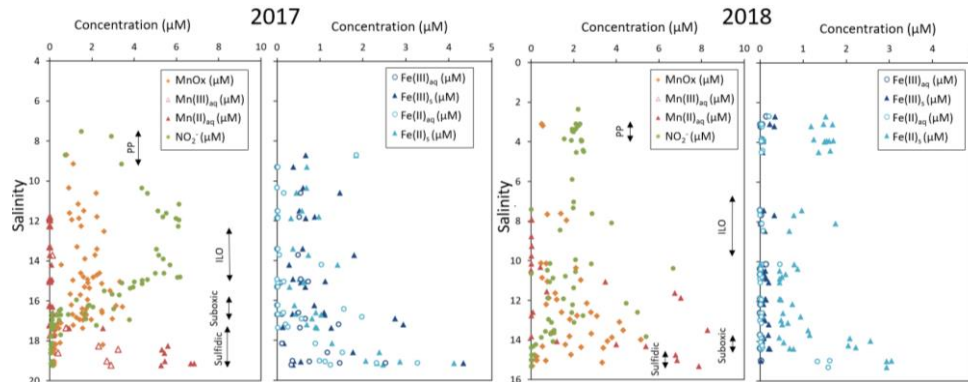

Figure 4: Mn, Fe and nitrite profiles build by superimposition of 11 casts for each campaign.

~~MnOx by H_2S. The increase of total manganese concentration with depth may result from sedimentary efflux or dissolved manganese trapping in more stagnant bottom water.~~A3. The primary production zone is depleted in dissolved Mn(II) and Mn(III), and shows an average value for solid MnOx ($0.7 \pm 0.1 \mu M$, n=4) and NO_2^- ($2.1 \pm 0.1 \mu M$, n=18). In 2018, iron speciation was investigated in the primary production zone showing an important iron pool ($1.6 \pm 0.1 \mu M$, n=9) dominated by solid Fe(II) ($95 \pm 2\%$). Below, in the ILO zone, NO_2^- reaches a maximum plateau at $5.3 \pm 0.2 \mu M$, n=11 in 2017 that is not visible in 2018, MnOx dominates the Mn pool in the ILO zone with concentration of $1.8 \pm 0.1 \mu M$, n=14 in 2017 and $1.3 \pm$

13

0.2 µM, n=3 in 2018). Fe(II) represents only 49% ± 13, n=4 of the iron pool (for a total iron concentration of 2.0 ± 0.4 µM, n=4) in 2017 while it represents 87 ± 5%, n=4 of the iron pool in 2018 (for a total concentration of 1.2 µM ± 0.2, n=4). Just

285   below oxygen depletion, in the suboxic zone, MnOx reaches a maximum (2.0 ± 0.1 µM, n=25 in 2017 and 2.9 ± 0.4 µM, n=12 in 2018). During both campaigns, the sulfidic layer is characterised by the absence of NO_2^- and MnOx while dissolved
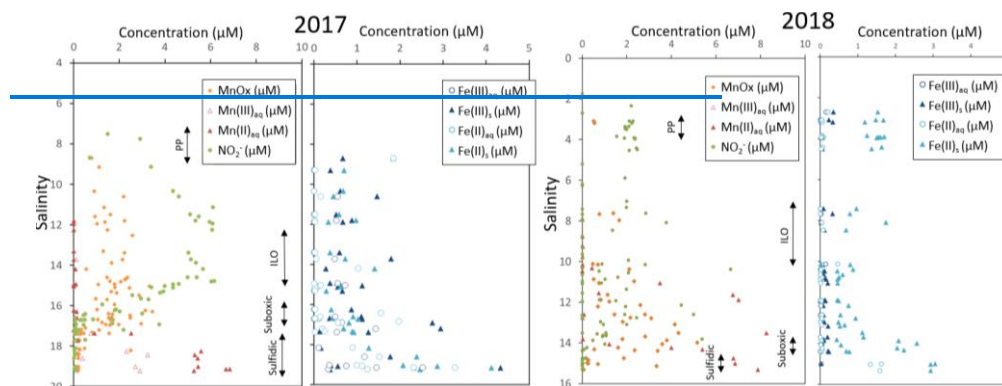
Figure 2: Mn, Fe and nitrate profiles build by superimposition of 11 casts for each campaign.

manganese concentration increases up to 7.7 ± 0.8 µM, n=15 and the iron pool increases to 5.0 ± 0.7 µM, n=13. No Mn(III) was detected with the porphyrin kinetics method (Thibault de Chanvalon and Luther, 2019) but about 30% of the total dissolved manganese flocculated after acidification down to pH 1.5 when analysed in 2017. Although similar recycling is expected for

290   iron, fresh precipitates are harder to catch due to higher particles content, and, in our study, lower dissolved total Fe concentration. Some features are discernible for a single cast (Fig. A2), but overall the only merging picture is an increase with proximity to the sediment interface for dissolved Fe(III) and Fe(II) and solid Fe(III) and Fe(II) (Fig. 2 indicating the existence of Mn(III).

3.2 River flow control

295   In rivers, the carbonate system equilibria depend on processes as varied as weathering intensity, draining bedrock and *in situ* biological activities. The inspection of dissolved inorganic carbon (DIC) changes versus total alkalinity (TA) changes is a frequent and efficient method to unravel the origin of these changes whereas other related parameters such as pCO_2 or pH are non-conservative during mixing and harder to interpret (*e.g.* Cai et al. 2017). However, due to river mixing with ocean waters, both TA and DIC change with salinity (S) as observed in the Chesapeake Bay during our campaigns ($r^2>0.95$, Fig. A1). The

300   calculation of the excess of TA and DIC, named TAex and DICex (see section 2.3.1), is required to interpret further biogeochemical processes (Su et al., 2020b).
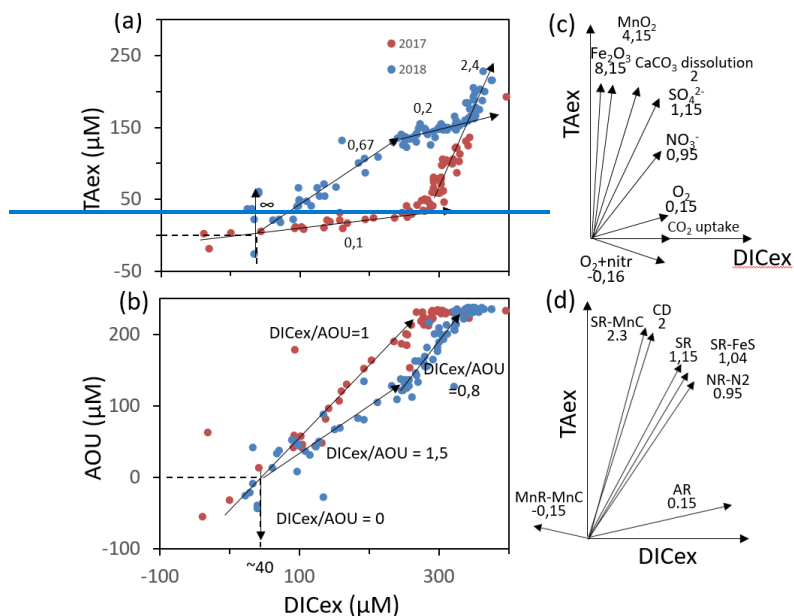
14

DICex increases progressively with depth up to about 330 µM and 350 µM at 25 m depth in 2017 and 2018 respectively (Fig. 1). The plot of TAex versus DICex (Fig. 3a) shows at the lowest observed salinity (7.1 in 2017 and 1.7 in 2018), an intercept for TAex = 0 corresponding to DICex ~ 40 µM. This offset is within the uncertainty of the endmember calculation even if slight DICex background enrichment has been modelled (Shen et al., 2019) resulting from faster atmospheric equilibration of O_2 than CO_2 after respiration reactions. Interestingly, the relative changes of DICex and TAex, further named ΔTAex and ΔDICex, does not depend on the endmember calculation and their ratio presents much lower uncertainties (about 0.1) facilitating their interpretation. In 2017, TAex stayed almost constant up to the oxic zone (Fig. 3a) with a ΔTAex/ΔDICex ratio of 0.1 ± 0.1 which indicates a net aerobic respiration (AR) (theoretical slope of ΔTAex/ΔDICex = 0.15 see Table 1 and Fig. 3c4. Discussion

The station 858 of the Chesapeake Bay shows very similar water column stratification between summer 2017 and summer 2018 despite a 10-folder differences in freshwater discharge rates (Fig. 3 and Fig. 4). Major features are: first, a surface layer characterized by intense atmospheric exchanges only sampled in 2018. Below, at about 3 meter depth, a subsurface layer associated with high primary production (PP zone) with high pH about 8, oversaturation of dioxygen and low CO_2 partial

15

315 pressure (down to 110 µatm). Below, a low oxygen layer with invariant concentration of most species surveyed (the invariant low oxygen (ILO) zone) is characterized by significant nitrite accumulation in 2017 (Fig. 4) probably due to oxidation of NH_4^+ diffusing upward and/or produced by *in situ* remineralisation. This feature is not visible in 2018 probably because the higher O_2 concentration in 2018 accelerates nitrite oxidation into nitrate and prevents any significant accumulation. Below, the suboxic zone, with neither O_2 nor H_2S detectable, is characterized by an increase of MnOx concentration and a pH minimum.

320 This MnOx maximum can be explained by the upward diffusing Mn^{2+} that is biologically oxidized by the downward diffusing O_2, even at low, undetectable, concentration (Clement et al., 2009). Additionally, Mn^{2+} could be oxidized by the nitrite or the nitrate (not measured) diffusing downward (thermodynamically favourable (Luther, 2010)). Compared to the ILO zone, the suboxic MnOx maximum corresponds to an increase of 0.2 µM in 2017, while it is much more marked in 2018 with an increase of 1.6 µM (Fig. 4). This difference could come from a faster Mn^{2+} oxidation produced by the steeper oxygen gradient above

325 the suboxic zone and by the thinness of the suboxic layer in 2018. Finally, in the deeper and sulfidic layer, the MnOx disappearance corresponds to the Mn^{2+} increases (Fig. 4) according to the reduction of settling MnOx by H_2S. The concentration increase of the manganese pool and of the iron pool with depth in the suboxic and sulfidic layers probably results from important sedimentary efflux.

4.1 Validity of the "reaction driven" interpretation in the context of station 858

330 The simultaneous and high-resolution sampling of multiple carbonate parameters and redox species gives us the rare opportunity to investigate in detail the interaction between carbonate species and redox sensitive elements. In the Chesapeake Bay, main changes of DIC and TA can be explained by mixing between upstream and oceanic endmembers (Appendix, Fig. A1). This "endmember driven" interpretation (see section 2.3.1), leads to the calculation of an excess of DIC and TA, DICex and TAex, relative to the mixing line and shown in Fig.5a. As detailed in section 2.3.1, these excesses can be explained either

335 by the occurring processes leading to a "reaction driven" (or spear) interpretation (Fig. 1b), or by mixing with an additional, third, endmember leading to an "endmember driven" (or hammer and bow) interpretation (Fig. 1a). In station 858, the steep gradient observed, for example the pH and pCO_2 gradient in the PP zone, the O_2 and NO_2^- gradient above the suboxic zone and the Mn, Fe and H_2S gradient at depth suggest that *ongoing in situ* processes control the changes of concentrations rather than the time-dependent endmember variability or the existence of an unknown third endmember. Additionally, the TAex

340 versus DICex plot (Fig. 5a) shows steep changes of direction while a preponderance of mixing would produce more progressive changes. Finally, at depth, Fig. 5a shows a similar slope for both years studied ($\Delta TAex/\Delta DICex = 2.4$) rather than a similar TAex and DICex concentration, which reinforces the validity of the "reaction driven" interpretation.
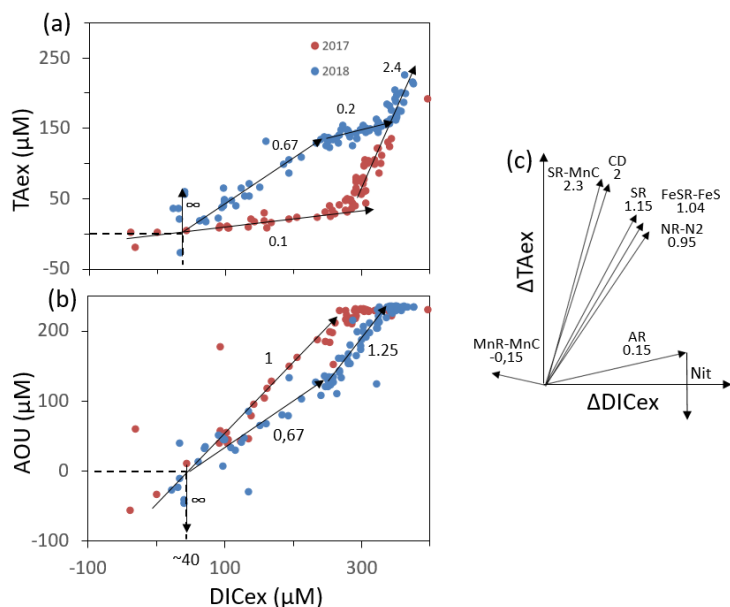
16

Figure 5: Description of the Taex/DICex/AOU system. (a) and (b) panels show samples measured along with interpretative slope discussed in the main text. Panel (c) shows the theoretical slope of TAex/DICex from combination of reactions presented in Table 1.

Assuming 1) that mixing is efficiently described by turbulent diffusion mixing, 2) that the measured concentrations correspond to a steady state – no gradient change over the 1 week sampling, 3) that the concentration at the starting point does not vary with time – as observed during one week sampling and 4) that the samples are isolated from atmospheric exchanges – sampling focus below 3 meters depth; the "reaction driven" interpretation (section 2.3.1) permits interpretation of the concentration changes as a linear combination of the stoichiometry of several chemical reactions (equation 5). The weighted coefficients of each reaction are equal to the rate of each reaction relative to the sum of the rate of all occurring reactions, v^i/v (equation 9). This interpretative framework describes the vertical stratification of the water column as the journey of a water mass slowly mixed deeper and deeper and whose DIC and TA are progressively enriched by all chemical reactions they undergo. Accordingly, this interpretation does not identify reactions with minor impact on the carbonate cycle or reactions cancelled later during the journey, for example, PP is frequently cancelled by similar amount or excess of AR. The starting point corresponds to the upstream (S=1.5) endmember at DICex=0; TAex=0. Figure 5a shows a slight DICex enrichment at TAex=0 which reflects a bias from the endmember calculation.

17

4.2 Identification of major reactions in oxygenated water column using ΔTAex/ΔDICex/ΔAOU signature.

In oxygenated water, the ΔTAex/ΔDICex analysis can be improved by looking also to the ΔAOU/ΔDICex ratio (Fig 5b) and establishing a ΔTAex/ΔDICex/ΔAOU signature for each water layer. Then, a linear combination of up to 3 reactions can be fit to the observed ΔTAex/ΔDICex/ΔAOU signature. The main candidate reactions to be combined are: aerobic respiration (AR), primary production (-AR), carbonate dissolution (CD) and nitrification of ammonium (Nit) as presented in the Table 1 and in Fig. 5c. In 2017, the whole oxygenated zone, including the PP zone and the ILO zone, is characterised by a ΔTAex/ΔDICex/ΔAOU = 0.1/1/1 (Fig. 5a and 5b) which corresponds to the occurrence of only net aerobic respiration (AR)

Table 1: Summary of the main net reactions occurring among the different zones of a redox gradient with reactants starting in equilibrium with the atmosphere. The calculations assume Redfield ratio of the organic matter, i. e. γN = 0.156 and γP = 0.0094 (Soetaert et al., 2007).

Name	Redox zones	Net Formula	ΔTA	ΔDIC
AR	Oxic	$(CH_2O)(NH_3)_{\gamma N}(H_3PO_4)_{\gamma P} + O_2 \rightarrow \gamma^N NH_3 + \gamma^P H_3PO_4 + CO_2 + H_2O$	0.15	+1
CD	Any	$CaCO_3 + CO_2 \rightarrow Ca^{2+} + 2 HCO_3^-$	2	+1
Nit	Oxic	$NH_3 + 2 O_2 \rightarrow HNO_3 + H_2O$	-2	0
NR-N2	Suboxic	$(CH_2O)(NH_3)_{\gamma N}(H_3PO_4)_{\gamma P} + 0.8 HNO_3 \rightarrow \gamma^N NH_3 + \gamma^P H_3PO_4 + CO_2 + 0.4 N_2 + 1.4 H_2O$	0.95	+1
NR-NH3	Suboxic	$(CH_2O)(NH_3)_{\gamma N}(H_3PO_4)_{\gamma P} + 0.5 HNO_3 \rightarrow \gamma^N NH_3 + \gamma^P H_3PO_4 + CO_2 + 0.5 NH_3 + 0.5 H_2O$	1.15	+1
MnR-MnC	Suboxic	$(CH_2O)(NH_3)_{\gamma N}(H_3PO_4)_{\gamma P} + 2 MnO_2 + CO_2 \rightarrow \gamma^N NH_3 + \gamma^P H_3PO_4 + 2 MnCO_3 + H_2O$	0.15	-1
SR	Sulfidic	$(CH_2O)(NH_3)_{\gamma N}(H_3PO_4)_{\gamma P} + 0.5 H_2SO_4 \rightarrow \gamma^N NH_3 + \gamma^P H_3PO_4 + CO_2 + 0.5 H_2S + H_2O$	1.15	+1
SR-SMnC	Sulfidic	$(CH_2O)(NH_3)_{\gamma N}(H_3PO_4)_{\gamma P} + 1/2 H_2SO_4 + 0.5 MnO_2 \rightarrow \gamma^N NH_3 + \gamma^P H_3PO_4 + 1/2 CO_2 + 1/2 MnCO_3 + 0.5 S^0 + 1.5 H_2O$	1.15	+0.5
FeSR-FeS	Sulfidic	$(CH_2O)(NH_3)_{\gamma N}(H_3PO_4)_{\gamma P} + 0.44 FeOOH + 0.44 H_2SO_4 \rightarrow \gamma^N NH_3 + \gamma^P H_3PO_4 + CO_2 + 0.44 FeS + 1.67 H_2O$	1.04	+1
SR-SFeS	Sulfidic	$(CH_2O)(NH_3)_{\gamma N}(H_3PO_4)_{\gamma P} + 0.33 FeOOH + 0.5 H_2SO_4 \rightarrow \gamma^N NH_3 + \gamma^P H_3PO_4 + CO_2 + 0.33 FeS + 0.17 S^0 + 1.67 H_2O$	1.15	+1
SR-FeS2	Sulfidic	$(CH_2O)(NH_3)_{\gamma N}(H_3PO_4)_{\gamma P} + 0.27 FeOOH + 0.53 H_2SO_4 \rightarrow \gamma^N NH_3 + \gamma^P H_3PO_4 + CO_2 + 0.27 FeS_2 + 1.67 H_2O$	1.21	+1

(theoretical value are 0.15/1/1 see Table 1 and Fig. 5c). ~~The AOU increase (Fig. 3b) confirms this possibility with a ΔDICex/ΔAOU signal similar to the expected theoretical slope of 1 for AR (Table 1).~~ Note that this ΔTAex/ΔDICex/ΔAOU

18

signature stands for absent or negligible nitrification following respiration. In case of full nitrification, the theoretical slopes should be $\Delta TA_{ex}/\Delta DIC_{ex}$ = ~~ /ΔAOU = -0.~~165~~ and $\Delta DIC_{ex}/\Delta AOU$ = 0.76~~167/1/1.31 as proposed by Zeebe and Wolf-Gladrow (2001). The absence of noticeable nitrification can be ~~explain~~explained by slow kinetics of NH_4^+ oxidation, with a half-life time estimated between a few days in estuaries (Horrigan et al., 1990) to multiple years in coastal environments (Heiss and Fulweiler, 2016). As a comparison, other NH_4^+ fates, such as adsorption leads to ammonium half life time of about a few minutes (Alshameri et al., 2018) to a few hours (Raaphorst and Malschaert, 1996) depending on the concentration of fine particles. Additionally, algae are known to use NH_4^+ as a N source (Raven et al., 1992) and NH_4^+ can be directly assimilated by heterotrophic organisms. ~~Finally, for 2017, despite pCO₂ being below atmospheric saturation at about 2 m depth (Fig. 1),~~

Table 2: Linear combination of reactions from Table 1 that fit the observations (see text for details, H_2O molecules are omitted).

	Linear combination (for 1 CH$_2$O)	ΔTA_{ex} / ΔDIC_{ex}	$\Delta AOU/\Delta DIC_{ex}$ or ΔH_2S / ΔDIC_{ex}	Net Formula (for 1 CH$_2$O)
Observed in 2018 — Oxic	AR	0.15	1	$(CH_2O)(NH_3)_{\gamma N}(H_3PO_4)_{\gamma P} + O_2 \rightarrow \gamma^N\,NH_3 + \gamma^P\,H_3PO_4 + CO_2$
	CD-AR	∞	-∞	$\gamma^N\,NH_3 + \gamma^P\,H_3PO_4 + CaCO_3 + 2\,CO_2 \rightarrow (CH_2O)(NH_3)_{\gamma N}(H_3PO_4)_{\gamma P} + O_2 + Ca^{2+} + 2\,HCO_3^-$
	AR+0.5CD	0.77	0.67	$(CH_2O)(NH_3)_{\gamma N}(H_3PO_4)_{\gamma P} + O_2 + 0.5\,CaCO_3 \rightarrow \gamma^N\,NH_3 + \gamma^P\,H_3PO_4 + 0.5\,CO_2 + 0.5\,Ca^{2+} + HCO_3^-$
	AR + 0.54 CD + 0.46 Nit	0.2	1.25	$(CH_2O)(NH_3)_{\gamma N}(H_3PO_4)_{\gamma P} + 1.93\,O_2 + 0.54\,CaCO_3 + 2\,\gamma_N\,NH_3 \rightarrow 3\gamma^N\,HNO_3 + \gamma^P\,H_3PO_4 + 0.46\,CO_2 + 0.54\,Ca^{2+} + 1.1\,HCO_3^-$
Observed in 2017 — Suboxic	0.98 SR-MnC + 0.02 MnR-MnC	2.4	0	$(CH_2O)(NH_3)_{\gamma N}(H_3PO_4)_{\gamma P} + 0.49\,H_2SO_4 + 0.53\,MnO_2 \rightarrow \gamma^N\,NH_3 + \gamma^P\,H_3PO_4 + 0.47\,CO_2 + 0.53\,MnCO_3 + 0.49\,S^0$
	0.65 SR-FeS + 0.35 MnR-MnC	2.4	0	$(CH_2O)(NH_3)_{\gamma N}(H_3PO_4)_{\gamma P} + 0.3\,H_2SO_4 + 0.7\,MnO_2 + 0.3\,FeOOH \rightarrow \gamma^N\,NH_3 + \gamma^P\,H_3PO_4 + 0.3\,CO_2 + 0.7\,MnCO_3 + 0.29\,FeS$
	6.4 CD + MnR-MnC	2.4	0	$(CH_2O)(NH_3)_{\gamma N}(H_3PO_4)_{\gamma P} + 6.4\,CaCO_3 + 2\,MnO_2 + 7.4\,CO_2 \rightarrow \gamma^N\,NH_3 + \gamma^P\,H_3PO_4 - 12.8\,HCO_3^- + 2\,MnCO_3 + 6.4\,Ca^{2+}$
Sulfidic	0.38 MnR-MnC + 0.76 SR – 0.15 SR-MnC	2.4	1.2	$(CH_2O)(NH_3)_{\gamma N}(H_3PO_4)_{\gamma P} + 0.31\,H_2SO_4 + 0.68\,MnO_2 + 0.07\,S^0 \rightarrow \gamma^N\,NH_3 + \gamma^P\,H_3PO_4 + 0.32\,CO_2 + 0.68\,MnCO_3 + 0.38\,H_2S$
	0.64 MnR-MnC + 1.36 SR – SR-MnC	2.4	3.2	$(CH_2O)(NH_3)_{\gamma N}(H_3PO_4)_{\gamma P} + 0.18\,H_2SO_4 + 0.79\,MnO_2 + 0.5\,S^0 \rightarrow \gamma^N\,NH_3 + \gamma^P\,H_3PO_4 + 0.21\,CO_2 + 0.79\,MnCO_3 + 0.68\,H_2S$

~~the possible CO₂ invasion does not significantly modify the observed ΔDICex/ΔAOU signal at the shallowest depth sampled.~~

19

In 2018, ~~this surface water history did not repeat as~~ fresh ~~and light~~ water masses brought by the exceptional flood ~~drastically~~ modified the carbonate system equilibrium. First, a low salinity layer with pCO_2 at ~~1000~~1540 µatm overlays the primary production layer (Fig. ~~1~~3), preventing the uptake of atmospheric CO_2 by primary production as was observed ~~for other years~~in 2016 (Chen et al., 2020). Just below the ~~air-sea interface~~surface layer, in the PP zone, the lock down of atmospheric exchanges by the ~~law~~low salinity layer produces supersaturation of trapped O_2 (Fig. ~~1, for S between~~3 ~~and 4~~). In Fig. ~~3a~~5a and ~~3b~~5b, this process translates into a vertical distribution at $DICex = 40$ µM associated with negative AOU and slightly positive TAex~~.~~, i.e. a $\Delta TAex/\Delta DICex/\Delta AOU = \infty/0/-\infty$. This original signature can be modelled by the combination of simultaneous carbonate

~~Table 1: Summary of the main net reactions occurring among the different zones of a redox gradient with reactants starting in equilibrium with the atmosphere, adapted from Soetaert et al. (2007). The calculations assume Redfield ratio of the organic matter, i. e. $\gamma N = 0.156$ and $\gamma P = 0.0094$ (Soetaert et al., 2007). Redox zones describe the different conditions required for completing the reaction.~~

~~Name~~	~~Redox zones~~	~~Net Formula~~	~~ΔTA~~	~~ΔDIC~~
~~AR~~	~~Oxic~~	~~$(CH_2O)(NH_3)_{\gamma N}(H_3PO_4)_{\gamma P} + O_2 \rightarrow \gamma^N NH_3 + \gamma^P H_3PO_4 + CO_2 + H_2O$~~	~~0.15~~	~~+1~~
~~CD~~	~~Any~~	~~$CaCO_3 + CO_2 \rightarrow Ca^{2+} + 2\ HCO_3^-$~~	~~2~~	~~+1~~
~~NR-N2~~	~~Suboxic~~	~~$(CH_2O)(NH_3)_{\gamma N}(H_3PO_4)_{\gamma P} + 0.8\ HNO_3 \rightarrow \gamma^N NH_3 + \gamma^P H_3PO_4 + CO_2 + 0.4\ N_2 + 1.4\ H_2O$~~	~~0.95~~	~~1~~
~~MnR-MnC~~	~~Suboxic~~	~~$(CH_2O)(NH_3)_{\gamma N}(H_3PO_4)_{\gamma P} + 2\ MnO_2 + CO_2 \rightarrow \gamma^N NH_3 + \gamma^P H_3PO_4 + 2\ MnCO_3 + H_2O$~~	~~0.15~~	~~-1~~
~~SR~~	~~Sulfidic~~	~~$(CH_2O)(NH_3)_{\gamma N}(H_3PO_4)_{\gamma P} + 1/2\ H_2SO_4 \rightarrow \gamma^N NH_3 + \gamma^P H_3PO_4 + CO_2 + 1/2\ H_2S + H_2O$~~	~~1.15~~	~~+1~~
~~SR-O~~	~~Sulfidic + Oxic~~	~~$(CH_2O)(NH_3)_{\gamma N}(H_3PO_4)_{\gamma P} + 1/2\ H_2SO_4 + O_2 \rightarrow \gamma^N NH_3 + \gamma^P H_3PO_4 + CO_2 + 1/2\ H_2SO_4 + H_2O$~~	~~0.15~~	~~+1~~
~~SR-MnC~~	~~Sulfidic + Suboxic~~	~~$(CH_2O)(NH_3)_{\gamma N}(H_3PO_4)_{\gamma P} + 1/2\ H_2SO_4 + 0.5\ MnO_2 \rightarrow \gamma^N NH_3 + \gamma^P H_3PO_4 + 1/2\ CO_2 + 1/2\ MnCO_3 + 0.5\ S^0 + 1.5\ H_2O$~~	~~1.15~~	~~+0.5~~
~~SR-FeS~~	~~Sulfidic + Suboxic~~	~~$(CH_2O)(NH_3)_{\gamma N}(H_3PO_4)_{\gamma P} + 0.44\ FeOOH + 0.44\ H_2SO_4 \rightarrow \gamma^N NH_3 + \gamma^P H_3PO_4 + CO_2 + 0.44\ FeS + 1.67\ H_2O$~~	~~1.04~~	~~+1~~

dissolution (CD~~)~~), the water column being undersaturated, and PP fuelled by NH_4^+, in equal proportion ~~and would result in no DICex, only TAex production (see~~2nd line in Table 2); the carbonate dissolution buffers the DIC consumption produced by PP. ~~The Ca^{2+} concentrations observed by Su et al. (2021) and during the 2018 cruise (data not shown) vary linearly with salinity i. e. $[Ca^{2+}] = 0.282\ S + 0.4$ in mmol L^{-1}. Assuming similar behaviour in 2017, calculations show that the whole water column is undersaturated with respect to calcite and validates the possibility for CD.~~

20

In 2018, below the PP zone down to DICex = 240µM, the beginning of the ILO zone, the TAex increases significantly with a ΔTAex/ΔDICex signature incompatible with AR (ΔTAex/ΔDICex=0.67 ± 0.1, Fig. 3A) and a ΔDICex/ΔAOU close to 1.5. Although there are other available candidates, a contribution of CD superimposed on AR seems most likely (theoretical
390 ΔTAex/ΔDICex slope of 2 for CD, Table 1). A linear combination fitting leads to TA contribution of 13% from AR and 87% from CD (Table 2) and results in ΔTAex/ΔDICex = 0.77 and ΔDICex/ΔAOU = 1.5. An explanation of its occurrence solely in 2018 could be particularly carbonate rich suspended material at high flow conditions. Deeper, in the ILO zone, the relations of ΔTAex/ΔDICex/ΔAOU (Fig. 3) result from aerobic respiration with almost indiscernible carbonate precipitation (ΔTAex/ΔDICex = 0.2, ΔDICex/ΔAOU = 0.8). Overall, our results show that the higher river flow of 2018 increases carbonate

Table 2: Linear combination of reactions from Table 1 that fit the observations (see text for details, H₂O molecules are omitted).

		Linear combination (for 1 CH₂O)	ΔTAex / ΔDICex	ΔDICex / AOU or ΔTAex / ΔH2S	Net Formula (for 1 mole of CH₂O)
Observed in 2018	Oxic	CD-AR	∞	0	γ^N NH₃ + γ^P H₃PO₄ + CaCO₃ + 2 CO₂ + 2 H₂O → (CH₂O)(NH₃)$_{\gamma N}$(H₃PO₄)$_{\gamma P}$ + O₂ + Ca²⁺ + 2 HCO₃⁻
		AR+0.5CD	0.77	1.5	(CH₂O)(NH₃)$_{\gamma N}$(H₃PO₄)$_{\gamma P}$ + O₂ + 0.5 CaCO₃ → γ^N NH₃ + γ^P H₃PO₄ + 0.5 CO₂ + 0.5 Ca²⁺ + HCO₃⁻
		AR	0.15	1	(CH₂O)(NH₃)$_{\gamma N}$(H₃PO₄)$_{\gamma P}$ + O₂ → γ^N NH₃ + γ^P H₃PO₄ + CO₂
Observed in 2017	Suboxic	0.98 SR-MnC + 0.02 MnR-MnC	2.4		(CH₂O)(NH₃)$_{\gamma N}$(H₃PO₄)$_{\gamma P}$ + 0.49 H₂SO₄ + 0.53 MnO₂ → γ^N NH₃ + γ^P H₃PO₄ + 0.47 CO₂ + 0.53 MnCO₃ + 0.49 S⁰
		0.65 SR-FeS + 0.35 MnR-MnC	2.4		(CH₂O)(NH₃)$_{\gamma N}$(H₃PO₄)$_{\gamma P}$ + 0.3 H₂SO₄ + 0.7 MnO₂ + 0.3 FeOOH → γ^N NH₃ + γ^P H₃PO₄ + 0.3 CO₂ + 0.7 MnCO₃ + 0.29 FeS
		6.4 CD + MnR-MnC	2.4		(CH₂O)(NH₃)$_{\gamma N}$(H₃PO₄)$_{\gamma P}$ + 6.4 CaCO₃ + 2 MnO₂ + 7.4 CO₂ → γ^N NH₃ + γ^P H₃PO₄ + 12.8 HCO₃⁻ + 2 MnCO₃ + 6.4 Ca²⁺
	Sulfidic	0.38 MnR-MnC + 0.76 SR - 0.15 SR-MnC	2.4	2	(CH₂O)(NH₃)$_{\gamma N}$(H₃PO₄)$_{\gamma P}$ + 0.31 H₂SO₄ + 0.68 MnO₂ + 0.07 S⁰ → γ^N NH₃ + γ^P H₃PO₄ + 0.32 CO₂ + 0.68 MnCO₃ + 0.38 H₂S
		0.64 MnR-MnC + 1.36 SR - SR-MnC	2.4	0.75	(CH₂O)(NH₃)$_{\gamma N}$(H₃PO₄)$_{\gamma P}$ + 0.18 H₂SO₄ + 0.79 MnO₂ + 0.5 S⁰ → γ^N NH₃ + γ^P H₃PO₄ + 0.21 CO₂ + 0.79 MnCO₃ + 0.68 H₂S

395 dissolution for the top 5-10 m depth (at salinity below 8) that superimpose on primary production (for salinity below 4) or aerobic respiration (for salinity between 4 and 8).3.3. Sediment control

21

3.3.1In 2018, below the PP zone down to DICex = 240μM, the beginning of the ILO zone, the TAex increases significantly with a $\Delta TAex/\Delta DICex/\Delta AOU = 0.67/1/0.67$ (Fig. 5a and 5b), incompatible with AR. To explain this signature a contribution of CD superimposed on AR seems most likely. A linear combination fitting leads 0.5 CD for 1 AR (3rd line in Table 2) and results in $\Delta TAex/\Delta DICex/\Delta AOU = 0.77/1/0.67$. An explanation of its occurrence solely in 2018 could be the increase in carbonate rich suspended material at high flow conditions (Su et al., 2021). Excess of Ca^{2+} compared to the mixing line with oceanic end member (not shown) indicate that up to 200 µM of Ca^{2+} is produced in the oxygenated layer. Deeper, in the ILO zone, $\Delta TAex/\Delta DICex/\Delta AOU = 0.2/1/1.25$ (Fig. 5a and 5b) results mainly from AR (0.15/1/1) with possible addition of CD and Nit, the exact signature being fitted for 0.54 CD and 0.46 Nit for 1 AR (4th line in Table 2), in close continuity of AR and CD relative rates from the overlaying layer. This important nitrification is also in good agreement with the lack of nitrite build up in the ILO zone and the relatively high oxygen concentration (at 105 µM) in the ILO zone in 2018 which is able to sustain nitrification. Overall, our results show that the higher river flow of 2018 increases carbonate dissolution for the top 5-10 m water depth that is superimposed on primary production or aerobic respiration. Additionally, in 2017 the $\Delta TAex/\Delta DICex/\Delta AOU$ system was undiscernible from the AR signature without nitrification, while in 2018 some nitrification in the ILO zone is suggested by the "reaction driven" interpretation.

4.3 Identification of ~~preponderant reactions~~major reactions in the anoxic water column using $\Delta TAex/\Delta DICex/\Delta H_2S$ signature.

~~In the absence of oxygen, in the suboxic and sulfidic zone, both campaigns show a similar evolution of the TAex and DICex with very high $\Delta TAex/\Delta DICex$ of 2.4 (Fig. 3a). This exceptionally high ratio, never reported in the literature, cannot be explained by most typical chemical reactions such carbonate dissolution (CD), aerobic respiration (AR), CO_2 uptake or primary production (PP = -AR). A scenario combining sulfate reduction (SR) is particularly attractive since SR represents the main carbon remineralisation pathway in absence of oxygen. However, a combination of SR with CD would result in a $\Delta TAex/\Delta DICex$ between 1.15 and 2 (see Table 1 or Fig. 3c) and fails to reach the $\Delta TAex/\Delta DICex$ of 2.4. Moreover, SR alone underestimates the importance of the H_2S oxidation pathway. H_2S oxidation is critical in the Chesapeake Bay since no H_2S is measurable in the suboxic zone while the gradient at the sediment/water interface indicates high H_2S sedimentary efflux (Fig. 1) and that oxidation can consume all the alkalinity produced during SR, as with oxygenated oxidation (see reaction SR-O in Table 1).~~

~~Generalizing these observations, recent efforts to build an alkalinity budget on the global scale (Hu and Cai, 2011; Middelburg et thal., 2020) highlight that the alkalinity produced by anaerobic respiration corresponds to the uncharged species produced, mostly in solid or gaseous phases. Indeed, the alkalinity changes produced during a natural reaction equal the "charges transfer" from species having some charge at pH = 4.5, such as NO_3^- and SO_4^{2-}, to "acid active species" that would lose its charges at pH = 4.5, mainly HCO_3^-, that does not count in the alkalinity calculation (see Eq. (4)).~~In the absence of oxygen, the $\Delta TAex/\Delta DICex/\Delta H_2S$ will be used for rates calculation. In the suboxic zone, the signature is similar in summer 2017 and 2018 at $\Delta TAex/\Delta DICex/\Delta H_2S = 2.4/1/0$. The "reaction driven" interpretation of this signature is more difficult than

22

430 in oxidized water because more reactions are known to occur simultaneously in absence of oxygen. However, it is not necessary to describe each reaction step but only the overall changes concerning the journey of a water mass over different redox conditions resulting in combined reaction. This approach has recently been proposed for FeS burial by Hiscock and Millero (2006), Rassmann et al. (2020) or Su et al. (2020b). A scenario combining sulfate reduction (SR) is particularly attractive since SR represents the main carbon remineralisation pathway in absence of oxygen. However, a combination of SR with CD would

435 result in a $\Delta TAex/\Delta DICex$ between 1.15 and 2 (see Table 1 or Fig. 5c) and fails to reach the $\Delta TAex/\Delta DICex$ of 2.4. Moreover, SR alone underestimates the importance of the H_2S oxidation pathway that can consume all the alkalinity produced during SR. For example, SR follow by oxygenated oxidation results in $\Delta TAex/\Delta DICex/\Delta AOU$ signature equal to AR only. In the Chesapeake Bay, H_2S oxidation is critical since no H_2S is measurable in the suboxic zone while the gradient at the sediment/water interface indicates high H_2S sedimentary efflux (Fig. 3).

440   Generalizing these observations, recent efforts to build an alkalinity budget on the global scale (Hu and Cai, 2011; Middelburg et al., 2020) highlight that the alkalinity produced by anaerobic respiration corresponds to the uncharged species produced, mostly in solid or gaseous phases. Indeed, the alkalinity changes produced during a natural reaction equal the "charge transfer" from species having some charge at pH = 4.5, such as NO_3^- and SO_4^{2-}, to species that would lose its charges at pH = 4.5, mainly HCO_3^-, that is not counted in the alkalinity calculation (see Eq. (12)). Although correct, this approach tends to

445 neglect the roles of Fe and Mn oxides (Middelburg et al., 2020) since their transformation from (oxyhydr)oxides into sulphur or carbonate species does not involve any charge transfer. When looking in detail at these processes, the metal oxides are critical since they are the main H_2S oxidation pathway that does not regenerate H_2SO_4 but rather produces S^0, S_n^{2-} or FeS (Findlay et al., 2014; Avetisyan et al., 2021) which limits alkalinity consumption.

     To build a pool of candidate reactions for the fitting, first, dissolved species ~~Although correct, this approach tends to neglect~~

450 ~~the roles of Fe and Mn oxides (Middelburg et al., 2020) since their transformation from (oxyhydr)oxides into sulphur or carbonate species does not involve any charge transfer. When looking in detail at these processes, the metal oxides are critical since they are the main H_2S oxidation pathway that does not regenerate H_2SO_4 but rather produces S^0 instead (Findlay et al., 2014; Avetisyan et al., 2021) which limits alkalinity consumption. The plot of selected redox sensitive species against TAex (Fig. 4) reveals a particular behaviour of MnOx in the suboxic water with a maximum concentration at the disappearance of~~

455 ~~O_2 followed by a decrease down to zero in presence of H_2S. Manganese changes from MnOx to Mn^{2+}, and ultimately to $MnCO_3$, consuming DIC and transforming H_2S to a non-charged species. This TA source is generally overlooked but may be important in the Chesapeake Bay. Fig. 2 and 4 also depict recycling of NO_2^- whose concentrations increase simultaneously to O_2. However, the small vertical shift between NO_2^- and O_2 minimum (Fig. 4) and the lack of overlap between NO_2^- and H_2S indicates that NO_2^- does not directly oxidize H_2S. Since, NH_4^+ and NO_3^- concentration were not measured, we limit our~~

460 ~~reasoning to the layer depleted in NO_2^-, that signals the negligible role of N cycling at these depths.~~
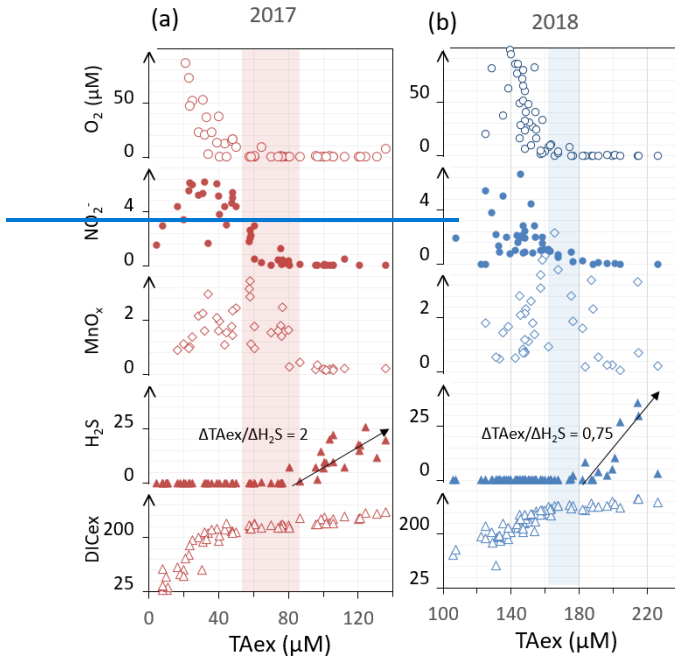
23

Figure 4: Evolution of selected species versus TAex for the 2017 (a) and 2018 (b) campaigns with the suboxic zone colored.

In the anoxic layer, most of the dissolved species are at too low concentration (*e.g.* Mn^{2+}_{aq}, Fe^{2+}_{aq}) to be a net reagent to affect the carbon cycle on a monthly time scale. at steady state are not taken into account. These species are usually recycled rapidly and hold a role of catalyser or electron shuttle between other redox species. Second, many minerals are expected to be at low concentration or thermodynamically not favoured, and their associated reactions are neglected (*e.g.,* iron phosphate, ferrous or manganous oxide, sulphur clusters, MnS, $FeCO_3$, adsorption processes, reverse weathering). Therefore, to explain the 100 μM TAex increase in absence of oxygen (Fig. 3a), only aqueous species with "important" stock concentrations at a monthly timescale (with concentrations that frequently (that can exceed 0.1 mM in anoxic porewaterwater) are taken into account, *i. e.,* SO_4^{2-}, Ca^{2+}, H_2S, NH_4^+ together with gaseous (N_2, CO_2) and main solid phases (FeS_2, FeS, S^0, $MnCO_3$, FeOOH, MnO_2). Based on these species, we detailed the most likely preponderant reactions for each redox zone (Table 1), although, for the sake of simplicity, many mineral and associated reactions are neglected (*e.g.,* iron phosphate, ferrous or manganous oxide, sulphur clusters, adsorption processes, reverse weathering). Third, many combinations of the carbon remineralisation

24

reaction with a re-oxidation reaction are equal to another remineralisation reaction. As an example, SR followed by H_2S oxidation with oxygen is equal to aerobic respiration.

Table 1 lists the resulting combined reactions and the calculated $\Delta TAex/\Delta DICex$ slopes are represented in Fig. 5c. For the suboxic zone, the nitrite reduction nitrate respiration can be associated with N_2 production or denitrification (NR-N2, Table 1) or with NH_3 production (NR-NH3) and the manganese oxides reduction associated with manganese respiration produces carbonates precipitation (MnR-MnC, Table 1) represent the main expected respiration processes. The reduction of HNO_3 down to NH_3 is not detailed but would result in almost similar alkalinity changes: 1.15 for NH_3 production (DNRA) versus 0.95 for N_2 production. The only solid form of Mn(II) is $MnCO_3$, since MnS is negligible despite thermodynamic possibilities. $FeCO_3$ production would produce a very similar reaction as $MnCO_3$ production; the latter, more common, is favoured in this simple description. Accordingly, the only solid). For the sulfidic zone, SR can occur alone producing a build-up of H_2S. However, at a certain point, H_2S gets significantly oxidised either by MnO_2 which produces $MnCO_3$ and S_0 (SR-MnC) or by FeOOH, producing FeS and S_0 (SR-SFeS) and ultimately FeS_2 (SR-FeS2). Direct respiration of FeOOH is also taken into account, but as the only Fe product from iron reactions is FeS and requires a coupling between iron oxide respiration and the minimum required amount of sulfate reduction (equation SR FeS). However, FeS_2 is implicitly taken into account since it corresponds to FeS plus S_0 and a specific coupling of iron oxide respiration with sulfate reduction to produce FeS_2 would result in $\Delta TAex=1.21$ $molC^{-1}$ instead of $\Delta TAex=1.04$ $molC^{-1}$ when FeS is the final product (Table 1). After sulfate reduction, H_2S can also accumulate in the water (SR reaction) or be oxidized back to SO_4^{2-} (SR O is detailed as an example). Finally, SR MnC describes H_2S oxidation by MnO_2 into S_0. Table 1 illustrates the importance of metal oxide to generate amount of high alkalinity in the case of sulfate reduction. In particular, it is FeS or FeS_2 it has to be accompanied by some SR (FeSR-FeS). This exercise highlights that the higher $\Delta TAex/\Delta DICex$ obtained ratio is 2.3 which corresponds to a combination of sulfate reduction follow followed by Mn (or Fe) oxide reduction follow by and Mn (or Fe) carbonate precipitation, and is here illustrated by (SR-SMnC) which fits extremely well with the SR MnC reaction from Table signature $\Delta TAex/\Delta DICex/\Delta H_2S = 2.4/1$ /0 reported in the Chesapeake Bay.

3.3.2 Quantification However, other linear combination of reactions importance

In listed in Table 1 result in the absence of H_2S, the simplest combination leading to the observed $\Delta TAex/\Delta DICex$ of 2.4 ± /1/0 1 is to consider sulfide oxidation by MnOx and formation of $MnCO_3$ leading to the SR-MnC reaction (theoretical ratio of $\Delta TAex/\Delta DICex = 2.3$, see Table 1). More complex combinations to better fit the $\Delta TAex/\Delta DICex$ can be found graphically in Fig. 3d. Note here the arrows demonstrate signature. Figure 5c demonstrates that the slope of 2.4 can be obtained for any reaction in combination with MnR-MnC. Combinations without MnR-MnC, however, leads lead to a negative SR and are not considered despite a possible small participation of anoxygenic phototrophic (purple) bacteria (Findlay et al., 2015, 2017). Therefore, in the absence of nitrate, oxygen and H_2S, only a combination of MnR-MnC with SR-MnC (producing S^0, 5th line in Table 2), SR-FeS (producing FeS, 6th line in Table 2) or CD (releasing Ca^{2+}, 7th line in Table 2) gives the particularly high $\Delta TAex/\Delta DICex$ of 2.4. S_0 was not measured during our campaign, but it has been previously reported at this site (Findlay et

25

al., 2014); thus,, and the S_0 produced by SR-MnC can react with FeS to form FeS_2. TheAll the three identified combinations require a critical role of MnO_2 in agreement with the observed remobilization in the hypoxic zone (Fig.. Since Figure 4). However, since the Ca^{2+}-survey (Su et al. 2021) did not reveal a significant production in the Chesapeake Bay, and since the available data on iron speciation (Fig. 2) do does not indicate any clear reaction, for iron while the steep gradient of MnOx in proximity to the H_2S rich layer suggests reaction between MnOx and H_2S; the combination of MnR-MnC with SR-MnC is the most likely. (5th line in Table 2). Deeper, in the presence of sulphide, the $\Delta TAex/\Delta DICex/\Delta H_2S$ signature is 2.4/1/1.2 in 2017 and 2.4/1/3.2 in 2018 and can be explained by the same combination of reactions without oxidized SR to take into account the build-up of H_2S (Table 2).

4.4 Comparison with other studies

The high observed ratio of $\Delta TAex/\Delta DICex = 2.4$ seems very specific to the Chesapeake Bay. Moreover, the "reaction driven" interpretation can be applied to other published datasets for which the $\Delta TA/\Delta DIC/\Delta H_2S$ system can be calculated (Table 3). In the water column, most of the available datasets are not suitable for the "reaction driven" interpretation since either they focus on surface water where DIC and TA are strongly impacted by atmospheric exchanges or the water masses change too fast to consider that reactions dominate over water mixing. However, porewater measured in the Gulf of Mexico has $\Delta TAex/\Delta DICex/\Delta H_2S = 1.15/1/0.53$ (Hu et al., 2010) In the presence of H_2S, a closer look at the relation between ΔH_2S versus $\Delta TAex$ (Fig. 4) reveals an interannual variation of the $\Delta TAex/\Delta H_2S$ ratio changing from 2 in 2017 to 0.75 in 2018 whereas the theoretical ratio of SR is $\Delta TAex/\Delta H_2S = 2.3$ when no H_2S is oxidized. These observed ratios indicates either TAex consumption without H_2S oxidation or H_2S formation without TAex production. The retained combination should implicate at least SR, to produce the H_2S, and MnR-MnC, to increase the $\Delta TAex/\Delta DICex$ slope, but it also requires another reaction to decrease the $\Delta TAex/\Delta H_2S$ ratio. Since carbonate under saturation prevents carbonate precipitation, and no primary production

a mis en forme : Anglais (États-Unis)

Table 3: Overview of the $\Delta TA/\Delta DIC/\Delta H2S$ signature observed in different environments

Publication	Sample type	$\Delta TA/\Delta DIC/ \Delta H2S$ or $\Delta TA/\Delta DIC/ \Delta AOU$	ΔTA	Reaction driven interpretation
Hu et al., 2010	Gulf of Mexico sediment (slope)	1.15/1/0.53	+ 17 mM	SR
Lukawska-Matuszewska, 2016	Baltic Sea sediment	1.3/1/0.07	+ 15 mM	SR-FeS2
Rassmann et al., 2020	Rhone prodelta sediment	1/1/0	+ 56 mM	FeSR-FeS
Cai et al. 1998	Satilla estuary	2/1/ND	+ 0.2 mM	CD
Drupp et al. 2016	Oxygenated Hawai carbonate reef sands	0.86-0.91/1/ND	+ 1.5 mM	Not applicable*
Su et al. 2021	Chesapeake Bay water column	2/1/1.5 AOU	+0.4 mM	Not applicable**
		0.2/1/1 AOU	+0.05 mM	AR
		0.8/1/ND	+0.1 mM	NR-N2 or CD+Nit
Hiscock and Millero 2006	Western Black Sea water column	1.3/1/0.5	+1.2 mM	SR+?CD

*Lack of data on oxygen concentration prevent any interpretation. ** Important air-water exchange prevent any "reaction driven" interpretation.

525 is expected, the most likely source of H_2S is from S_8, although FeS_2 is also possible, as depicted in Table 2. From this equation, the main TA source is the absence of SO_4^{2-} regeneration after sulfate reduction whereas the second source is the nutrient release that accounts for 19% and 29% of the TA produced in 2017 and 2018, respectively. The alternative possibility of NH_4^+ oxidation by MnO_2 into N_2 (Mn anammox, (Luther et al., 1997; Thamdrup, 2012)) could also reduce the alkalinity without additional H_2S oxidation.

530 Based on the stoichiometry proposed, about 88 µM to 155 µM of MnO_2 are required to produce the 100 µM TAex increase observed (Fig. 3a), one order of magnitude higher than the observed MnOx concentration (Fig. 4). Based on an average concentration of 20 µmol g^{-1} of Mn in suspended particles, the 88 µM of MnO_2 would require a suspended material concentration of about 4.4 g L^{-1}, which is again one or two orders of magnitude higher than the 0.01 – 0.1 g L^{-1} usually found in the Chesapeake Bay. However, previous studies at this station (*e.g.,* Sholkovitz et al., 1992) explained the seasonality of

535 anoxia with an upward move of the redox front from the sediments to bottom waters during the start of summer. Accordingly, it is likely that the observed dissolved species, notably TAex and DICex, have not been produced in the water column but rather in the sediment during the year and then transported simultaneously with other reduced elements as the summer begin. Therefore, the 100 µM TA increase does not fit with the ambient Mn^{2+} or MnO_2 in the water column but rather with the $MnCO_3$ deposited in the sediment. The sedimentary solid Mn stock is about 10 mM (assuming a porosity of 0.8, a solid density of 2.6

540 and a Mn content of 20 µmol g^{-1}), which largely exceeds the 88 µM required to produce the 100 µM TAex increase.

At a global scale, beside its role on alkalinity, MnO_2 can also be a trap for CO_2 as proposed in this Urey-Ebelman (Urey, 1952, Eq. 5) like reaction (Eq.6):

as expected when sulfate reduction is associated with H_2S accumulation (SR reaction; $\Delta TAex/\Delta DICex/\Delta H_2S = 1.15/1/0.5$; Table 1). Similarly, Hiscock and Millero (2006) report $\Delta TAex/\Delta DICex/\Delta H_2S = 1.3/1/0.5$ in the Western Black Sea close to

545 the SR signature. In the Baltic Sea sediment, $\Delta TAex/\Delta DICex/\Delta H_2S = 1.3/1/0.07$ was reported (Lukawska-Matuszewska, 2016), which is close to the expected signature in case of important H_2S consumption by Fe oxides and precipitation as pyrite (SR-FeS2 reaction; $\Delta TAex/\Delta DICex/\Delta H_2S = 1.2/1/0$). In Rhone river prodelta sediments, the reported $\Delta TAex/\Delta DICex/\Delta H_2S$ is 1/1/0 that can be related to the 1/1/0 signature of FeSR-FeS (Table 1) that is expected in iron rich sediment with high sedimentation rate preventing FeS_2 formation in the pore water (Rassmann et al., 2020). In permeable, carbonate rich

550 sediments, the reported signature of $\Delta TAex/\Delta DICex/\Delta H_2S$ in Hawaii sands is 0.86/1/ND (Drupp et al., 2016). The lack of salinity and oxygen datasets prevents further model fits, but the $\Delta TAex/\Delta DICex$ is below 2.4. For oxygen depleted data from the whole Chesapeake Bay described in Su et al. (2020), the signatures are $\Delta TAex/\Delta DICex/\Delta AOU = 0.2/1/1$ in presence of oxygen (typical signature of AR) and 0.8/1/ND in absence of oxygen that could correspond to NR-N2 or a combination of CD+Nit. Overall, this bibliographic survey highlights the effectiveness of the reaction driven approach to identify preponderant

555 reactions controlling the carbon cycle and puts in perspective the originality of the $\Delta TAex/\Delta DICex/\Delta AOU$ signature of 2.4/1/0 observed in the Chesapeake Bay.

27

4.5 Local and global budget

While the "reaction driven" interpretation indicates a dominant role of the SR-MnC reaction; this possibility needs to be validated looking at the saturation state of rhodocrosite (main $MnCO_3$ mineral) and looking at the mass budget between MnOx consumed and TAex produced. The rhodocrosite saturation (Luo and Millero, 2003) is always below 0.3 which stands against the occurrence of *in situ* SR-MnC reaction. When inspecting the mass budget, the 88 µM to 155 µM of MnO_2 required to produce the 100 µM TAex increase observed (Fig. 5a) is one order of magnitude higher than the observed MnOx or Mn^{2+} concentration (Fig. 4). This mass budget discrepancy cannot be solved invoking suspended material since the 88 µM of MnO_2 would require a suspended material concentration of about 4.4 g L^{-1} (assuming an average concentration of 20 µmol g^{-1} of Mn), which is again one or two orders of magnitude higher than the 0.01 – 0.1 g L^{-1} usually found in the Chesapeake Bay (Cerco et al., 2013). Therefore the SR-MnC reaction does not happen in the water column of the Chesapeake Bay. However, it is likely that the TAex and DICex have rather been produced in the sediment during the previous year and then diffused simultaneously with other reduced elements as the summer begins. Indeed, previous studies at station 858 (*e.g.,* Sholkovitz et al., 1992) explained the seasonality of anoxia with an upward move of the redox front from the sediments to bottom waters during the start of summer. Important sedimentary efflux of H_2S, Fe_{aq} and Mn_{aq} were still visible during both August campaigns. Therefore, the 100 µM TA increase does not fit with the ambient Mn^{2+} or MnO_2 in the water column but rather with the $MnCO_3$ deposited in the sediment. The sedimentary solid Mn stock of the Chesapeake Bay is particularly important, up to 70 µmol g^{-1} at station 858 (Sinex and Helz, 1981) compared to an average value of 15 µmol g^{-1} for the upper continental crust (Rudnick and Gao, 2003). Indeed semi-enclosed basins are known to concentrate manganese at the deeper sediment (Thamdrup and Dalsgaard, 2000; Lenstra et al., 2020). Recent investigations at a close station (ET 5.1; 38°48.36'N; 75°54.66'W) in the Chesapeake Bay (Lenstra et al., 2021) report that about 60% of the surface sedimentary Mn pool is MnOx (acid ascorbic extractable) and 25 % is Mn carbonate (1M HCl extraction). Assuming a porosity of 0.8, a bulk solid density of 2.6, the sedimentary pool corresponds to 35 mM of manganese which largely exceeds the 88 µM required to produce the 100 µM TAex increase. Therefore, the Chesapeake Bay sediment is particularly rich in manganese and could host important SR-MnC reactions in the superficial pore water whose soluble products diffuse up to the water column during summer and could bear with them the high ΔTAex/ΔDICex signature observed.

At a global scale, beside its role on alkalinity, MnO_2 can also be a trap for CO_2 as proposed in this Urey-Ebelman (Urey, 1952, Eq. 13) like reaction (Eq.14):

$$SiCaO_3 + CO_2 \rightarrow SiO_2 + CaCO_3 \qquad (13)$$

$$MnO_2 + CO_2 \rightarrow 0.5\ O_2 + MnCO_3 \qquad (14)$$

Assuming all the Mn is in the form of MnO_2, a weathering intensity similar to iron (Poulton and Raiswell, 2002) and based on the upper continental crust composition (Rudnick and Gao, 2003), the continental MnO_2 input to the ocean can be estimated at 0.4 x 10^{12} mol y^{-1}. Assuming a steady state ocean toward Mn and $MnCO_3$ as the unique sedimentary phase, this estimation

28

~~represent~~represents 1.4 % of the total carbonate burial (Middelburg et al., 2020). Although negligible at the global scale, this carbonate burial may be significant in MnO_2 rich semi-enclosed basins.

Conclusion

The "reaction driven" interpretation identifies the major reactions controlling the carbonate cycle. In the Chesapeake Bay, similar redox stratification can support varying intensity of carbonate dissolution, absent in 2017 or important as in 2018. The summer anoxia observed in the Chesapeake Bay is characterized by ~~exceptional~~an exceptionally high $\Delta TAex/\Delta DICex$ of 2.4 which has never been reported in anoxic water columns or sediment pore waters. ~~By comparison, pore water $\Delta TAex/\Delta DICex$ was measured at 1.15 in the Gulf of Mexico~~The "reaction driven" interpretation suggests it comes from sulphate reduction follow by almost complete hydrogen sulphide oxidation by $MnOx$ followed by $MnCO_3$ precipitation. This interpretation is supported by the important manganese dynamics observed. However, the rhodocrosite saturation index is below 1, and the weak pool of manganese measured indicates that most of the reactions would have occurred in the upper pore water from which the $\Delta TAex/\Delta DICex$ of 2.4 would have diffused into the bottom water with the redox front during summer water column anoxia set up. Although~~,~~ ~~(Hu et al., 2010) with $\Delta TAex / \Delta H2S \sim 2.2$ as expected when sulfate reduction is associated with H_2S accumulation (theoretical $\Delta TAex / \Delta H2S$ ratio from SR being 2.3, Table 1). In the Baltic Sea, a $\Delta TAex/\Delta DICex$ ratio of 1.3 was reported (Lukawska-Matuszewska, 2016) with $\Delta TAex / \Delta H_2S > 17.5$, signs of important H_2S consumption by Fe oxides. In oxygenated coastal sediment, where dissolved reduced compounds are oxidised before release in the water columns, fluxes of TA over fluxes of DIC ranged from 0.4 to 1 (Rassmann et al., 2020 and references therein). In the Chesapeake Bay, $\Delta TAex / \Delta H_2S$ is below 2.3, a sign of another preponderant reaction. The stoichiometry analysis agrees with direct measurements to underline the critical role of MnO_2 reduction followed by Mn carbonate precipitation. This scenario could be confirmed by a careful analysis of Mn oxides concentration in the bottom sediment during the entire year, since semi-enclosed basins are known to concentrate manganese oxides into the deeper area during oxygenated conditions (Thamdrup and Dalsgaard, 2000; Madison et al., 2013; Lenstra et al., 2020). Despite the fact that~~ $MnCO_3$ production from MnO_2 involves no charge transfer (Hu and Cai, 2011), our study demonstrates that it can have strong impact on local alkalinity (Middelburg et al., 2020). The lack of charge transfer visible from the stoichiometry implies that Mn ~~has no bearing on~~does not bear the alkalinity it produces, but it is a critical element to limit the H_2S oxidation to its S_0 intermediate ~~form~~forms and finally to favour its burial.
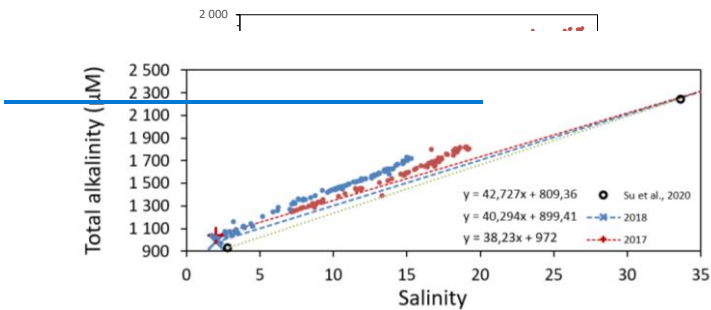
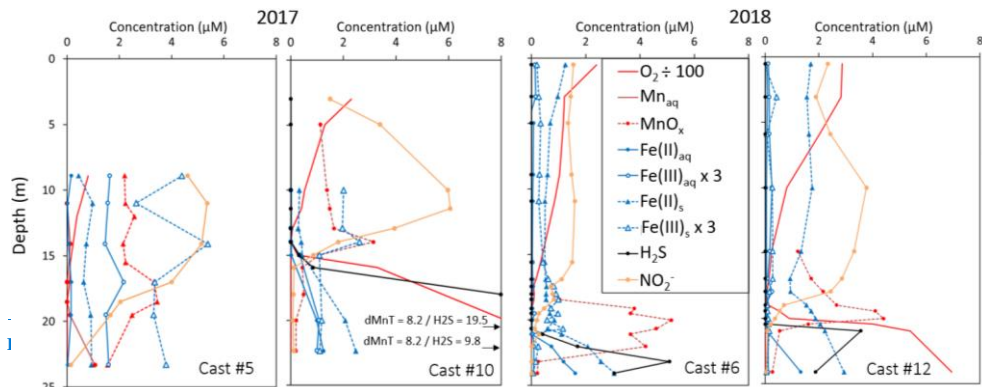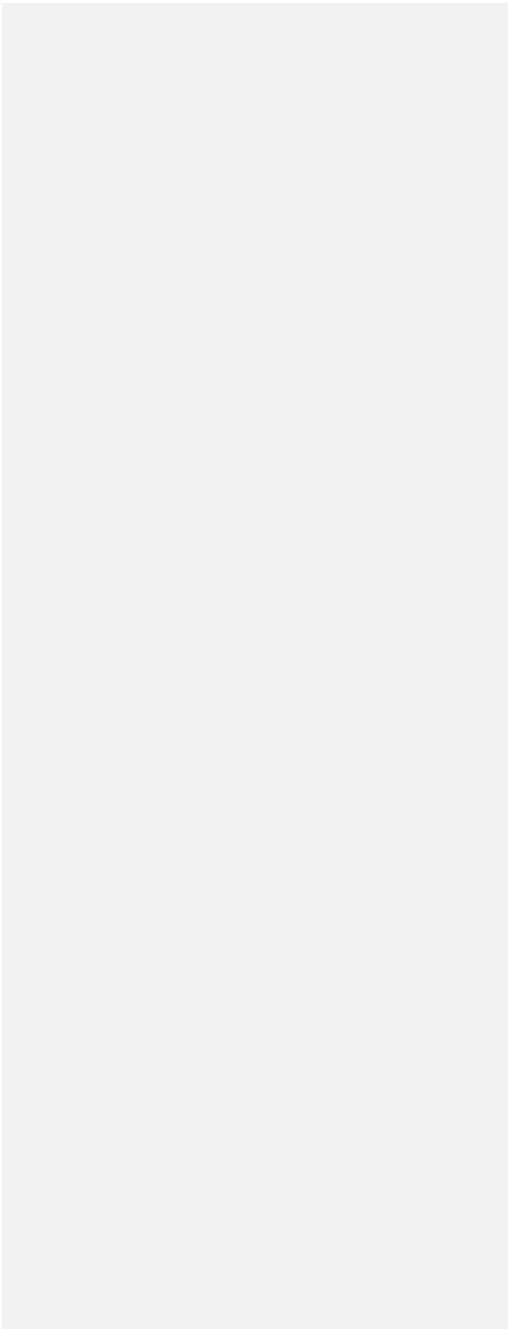a mis en forme : Anglais (États-Unis)

31

Appendix A

Figure A2: Examples of redox and metal chemistry profiles. Note that Fe(III)$_s$ and Fe(III)$_{aq}$ scales are zoomed in by 3 and O$_2$ scale is zoomed out by 100.
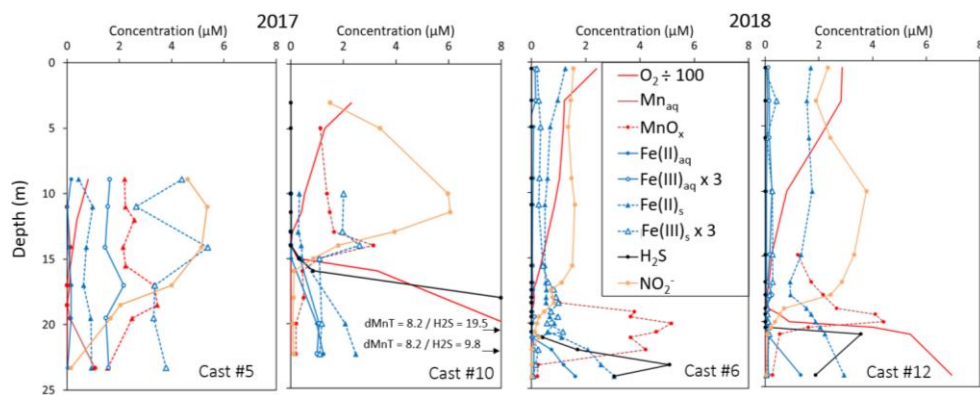
615

32

Figure A3: Examples of redox and metal chemistry profiles. Note that Fe(III)$_s$ and Fe(III)$_{aq}$ scales are zoomed in by 3 and O$_2$ scale is zoomed out by 100.

Data availability

The data used in this paper is available on request to the correspond author.

Author contribution

ATC, ERE, JN, BMT and SJ performed the data analysis. ATC and SJ process the data. ATC, GWL, SJ and WJC interpreted the results. GWL, BMT and WJC get the funding. ATC wrote the paper with contributions from all authors.

Competing interests

The authors declare that they have no conflict of interest.

References

Abril, G., Etcheber, H., Delille, B., Frankignoulle, M., and Borges, A. V.: Carbonate dissolution in the turbid and eutrophic Loire estuary, Mar. Ecol. Prog. Ser., 259, 129–138, 2003.

34

Alshameri, A., He, H., Zhu, J., Xi, Y., Zhu, R., Ma, L., and Tao, Q.: Adsorption of ammonium by different natural clay minerals: Characterization, kinetics and adsorption isotherms, Appl. Clay Sci., 159, 83–93, https://doi.org/10.1016/j.clay.2017.11.007, 2018.

635 Avetisyan, K., Zweig, I., Luther, G. W., and Kamyshny, A.: Kinetics and mechanism of polysulfides and elemental sulfur formation by a reaction between hydrogen sulfide and δ-MnO2, Geochim. Cosmochim. Acta, 313, 21–37, https://doi.org/10.1016/j.gca.2021.08.022, 2021.

Borges, A. V., Schiettecatte, L.-S., Abril, G., Delille, B., and Gazeau, F.: Carbon dioxide in European coastal waters, Estuar. Coast. Shelf Sci., 70, 375–387, https://doi.org/10.1016/j.ecss.2006.05.046, 2006.

640 Borges, A. V., Abril, G., and Bouillon, S.: Carbon dynamics and CO2 and CH4 outgassing in the Mekong delta, Biogeosciences, 15, 1093–1114, https://doi.org/10.5194/bg-15-1093-2018, 2018.

Boudreau, B. P., Middelburg, J. J., and Luo, Y.: The role of calcification in carbonate compensation, Nat. Geosci., 11, 894–900, https://doi.org/10.1038/s41561-018-0259-5, 2018.

Boyle, E., Collier, R., Dengler, A., Edmond, J., Ng, A., and Stallard, R.: On the chemical mass-balance
645 in estuaries, Geochim. Cosmochim. Acta, 38, 1719–1728, 1974.

Cai, W.-J., Huang, W.-J., Luther, G. W., Pierrot, D., Li, M., Testa, J., Xue, M., Joesoef, A., Mann, R., Brodeur, J., Xu, Y.-Y., Chen, B., Hussain, N., Waldbusser, G. G., Cornwell, J., and Kemp, W. M.: Redox reactions and weak buffering capacity lead to acidification in the Chesapeake Bay, Nat. Commun., 8, 369, https://doi.org/10.1038/s41467-017-00417-7, 2017.

650 Cai, W.-J., Xu, Y.-Y., Feely, R. A., Wanninkhof, R., Jönsson, B., Alin, S. R., Barbero, L., Cross, J. N., Azetsu-Scott, K., Fassbender, A. J., Carter, B. R., Jiang, L.-Q., Pepin, P., Chen, B., Hussain, N., Reimer, J. J., Xue, L., Salisbury, J. E., Hernández-Ayón, J. M., Langdon, C., Li, Q., Sutton, A. J., Chen, C.-T. A., and Gledhill, D. K.: Controls on surface water carbonate chemistry along North American ocean margins, Nat. Commun., 11, https://doi.org/10.1038/s41467-020-16530-z, 2020.

655 Cerco, C. F., Kim, S.-C., and Noel, M. R.: Management modeling of suspended solids in the Chesapeake Bay, USA, Estuar. Coast. Shelf Sci., 116, 87–98, https://doi.org/10.1016/j.ecss.2012.07.009, 2013.

Chen, B., Cai, W.-J., Brodeur, J. R., Hussain, N., Testa, J. M., Ni, W., and Li, Q.: Seasonal and spatial variability in surface pCO2 and air–water CO2 flux in the Chesapeake Bay, Limnol. Oceanogr., 65, 3046–3065, https://doi.org/10.1002/lno.11573, 2020.

660 Clement, B. G., Luther, G. W., and Tebo, B. M.: Rapid, oxygen-dependent microbial Mn(II) oxidation kinetics at sub-micromolar oxygen concentrations in the Black Sea suboxic zone, Geochim. Cosmochim. Acta, 73, 1878–1889, https://doi.org/10.1016/j.gca.2008.12.023, 2009.

Cotovicz Jr., L. C., Libardoni, B. G., Brandini, N., Knoppers, B. A., and Abril, G.: Comparisons between real-Time PCO2 measurements with indirect estimates in two contrasting Brazilian estuaries: The eutrophic guanabara bay (RJ) and the oligotrophic sao francisco River estuary (AL), Quím. Nova, 39, 1206–1214, https://doi.org/10.21577/0100-4042.20160145, 2016.

Dickson, A. G.: An exact definition of total alkalinity and a procedure for the estimation of alkalinity and total inorganic carbon from titration data, Deep Sea Res. Part Oceanogr. Res. Pap., 28, 609–623, https://doi.org/10.1016/0198-0149(81)90121-7, 1981.

Drupp, P. S., De Carlo, E. H., and Mackenzie, F. T.: Porewater CO2–carbonic acid system chemistry in permeable carbonate reef sands, Mar. Chem., 185, 48–64, https://doi.org/10.1016/j.marchem.2016.04.004, 2016.

Findlay, A. J., Gartman, A., MacDonald, D. J., Hanson, T. E., Shaw, T. J., and Luther, G. W.: Distribution and size fractionation of elemental sulfur in aqueous environments: The Chesapeake Bay and Mid-Atlantic Ridge, Geochim. Cosmochim. Acta, 142, 334–348, 2014.

Findlay, A. J., Bennett, A. J., Hanson, T. E., and Luther, G. W.: Light-Dependent Sulfide Oxidation in the Anoxic Zone of the Chesapeake Bay Can Be Explained by Small Populations of Phototrophic Bacteria, Appl. Environ. Microbiol., 81, 7560–7569, https://doi.org/10.1128/AEM.02062-15, 2015.

Findlay, A. J., Di Toro, D. M., and Luther, G. W.: A model of phototrophic sulfide oxidation in a stratified estuary, Limnol. Oceanogr., 62, 1853–1867, https://doi.org/10.1002/lno.10539, 2017.

Friedlingstein, P., Jones, M. W., O'Sullivan, M., Andrew, R. M., Hauck, J., Peters, G. P., Peters, W., Pongratz, J., Sitch, S., Le Quéré, C., Bakker, D. C. E., Canadell, J. G., Ciais, P., Jackson, R. B., Anthoni, P., Barbero, L., Bastos, A., Bastrikov, V., Becker, M., Bopp, L., Buitenhuis, E., Chandra, N., Chevallier, F., Chini, L. P., Currie, K. I., Feely, R. A., Gehlen, M., Gilfillan, D., Gkritzalis, T., Goll, D. S., Gruber, N., Gutekunst, S., Harris, I., Haverd, V., Houghton, R. A., Hurtt, G., Ilyina, T., Jain, A. K., Joetzjer, E., Kaplan, J. O., Kato, E., Klein Goldewijk, K., Korsbakken, J. I., Landschützer, P., Lauvset, S. K., Lefèvre, N., Lenton, A., Lienert, S., Lombardozzi, D., Marland, G., McGuire, P. C., Melton, J. R., Metzl, N., Munro, D. R., Nabel, J. E. M. S., Nakaoka, S.-I., Neill, C., Omar, A. M., Ono, T., Peregon, A., Pierrot, D., Poulter, B., Rehder, G., Resplandy, L., Robertson, E., Rödenbeck, C., Séférian, R., Schwinger, J., Smith, N., Tans, P. P., Tian, H., Tilbrook, B., Tubiello, F. N., van der Werf, G. R., Wiltshire, A. J., and Zaehle, S.: Global Carbon Budget 2019, Earth Syst. Sci. Data, 11, 1783–1838, https://doi.org/10.5194/essd-11-1783-2019, 2019.

Grasshoff, K.: Determination of nitrite, nitrate, oxygen, thiosulphate, in: Methods of seawater analysis, New York, 61–72, 1983.

Heiss, E. M. and Fulweiler, R. W.: Coastal water column ammonium and nitrite oxidation are decoupled in summer, Estuar. Coast. Shelf Sci., 178, 110–119, https://doi.org/10.1016/j.ecss.2016.06.002, 2016.

36

Hiscock, W. T. and Millero, F. J.: Alkalinity of the anoxic waters in the Western Black Sea, Deep Sea Res. Part II Top. Stud. Oceanogr., 53, 1787–1801, https://doi.org/10.1016/j.dsr2.2006.05.020, 2006.

Horrigan, S. G., Montoya, J. P., Nevins, J. L., McCarthy, J. J., Ducklow, H., Goericke, R., and Malone, T.: Nitrogenous nutrient transformations in the spring and fall in the Chesapeake Bay, Estuar. Coast. Shelf Sci., 30, 369–391, https://doi.org/10.1016/0272-7714(90)90004-B, 1990.

Hu, X. and Cai, W.-J.: An assessment of ocean margin anaerobic processes on oceanic alkalinity budget, Glob. Biogeochem. Cycles, 25, https://doi.org/10.1029/2010GB003859, 2011.

Hu, X., Cai, W.-J., Wang, Y., Luo, S., and Guo, X.: Pore-water geochemistry of two contrasting brine-charged seep sites in the northern Gulf of Mexico continental slope, Mar. Chem., 118, 99–107, https://doi.org/10.1016/j.marchem.2009.11.006, 2010.

Huang, W.-J., Wang, Y., and Cai, W.-J.: Assessment of sample storage techniques for total alkalinity and dissolved inorganic carbon in seawater, Limnol. Oceanogr. Methods, 10, 711–717, https://doi.org/10.4319/lom.2012.10.711, 2012.

Hudson, J. M., MacDonald, D. J., Estes, E. R., and Luther, G. W.: A durable and inexpensive pump profiler to monitor stratified water columns with high vertical resolution, Talanta, 199, 415–424, https://doi.org/10.1016/j.talanta.2019.02.076, 2019.

Ishii, H., Koh, H., and Satoh, K.: Spectrophotometric determination of manganese utilizing metal ion substitution in the cadmium-α, β,-γ, δ-tetrakis (4-carboxyphenyl) porphine complex, Anal. Chim. Acta, 136, 347–352, 1982.

Joesoef, A., Kirchman, D. L., Sommerfield, C. K., and Cai, W.-J.: Seasonal variability of the inorganic carbon system in a large coastal plain estuary, Biogeosciences, 14, 4949–4963, https://doi.org/10.5194/bg-14-4949-2017, 2017.

Jones, M. R., Luther, G. W., Mucci, A., and Tebo, B. M.: Concentrations of reactive Mn(III)-L and MnO2 in estuarine and marine waters determined using spectrophotometry and the leuco base, leucoberbelin blue, Talanta, 200, 91–99, https://doi.org/10.1016/j.talanta.2019.03.026, 2019.

Lenstra, W. K., Séguret, M. J. M., Behrends, T., Groeneveld, R. K., Hermans, M., Witbaard, R., and Slomp, C. P.: Controls on the shuttling of manganese over the northwestern Black Sea shelf and its fate in the euxinic deep basin, Geochim. Cosmochim. Acta, 273, 177–204, https://doi.org/10.1016/j.gca.2020.01.031, 2020.

Lenstra, W. K., Klomp, R., Molema, F., Behrends, T., and Slomp, C. P.: A sequential extraction procedure for particulate manganese and its application to coastal marine sediments, Chem. Geol., 120538, https://doi.org/10.1016/j.chemgeo.2021.120538, 2021.

37

Lewis, B. L., Glazer, B. T., Montbriand, P. J., Luther, G. W., Nuzzio, D. B., Deering, T., Ma, S., and
730 Theberge, S.: Short-term and interannual variability of redox-sensitive chemical parameters in hypoxic/anoxic bottom waters of the Chesapeake Bay, Mar. Chem., 105, 296–308, https://doi.org/10.1016/j.marchem.2007.03.001, 2007.

Lohrenz, S. E., Cai, W.-J., Chen, F., Chen, X., and Tuel, M.: Seasonal variability in air-sea fluxes of CO 2 in a river-influenced coastal margin, J. Geophys. Res., 115, 2010.

735 Lukawska-Matuszewska, K.: Contribution of non-carbonate inorganic and organic alkalinity to total measured alkalinity in pore waters in marine sediments (Gulf of Gdansk, S-E Baltic Sea), Mar. Chem., 186, 211–220, https://doi.org/10.1016/j.marchem.2016.10.002, 2016.

Luo, Y. and Millero, F. J.: Solubility of Rhodochrosite (MnCO3) in NaCl Solutions, J. Solut. Chem., 12, 2003.

740 Luther, G. W.: The role of one-and two-electron transfer reactions in forming thermodynamically unstable intermediates as barriers in multi-electron redox reactions, Aquat. Geochem., 16, 395–420, 2010.

Luther, G. W., Sundby, B., Lewis, B. L., Brendel, P. J., and Silverberg, N.: Interactions of manganese with the nitrogen cycle: alternative pathways to dinitrogen, Geochim. Cosmochim. Acta, 61, 4043–4052, 1997.

745 Madison, A. S., Tebo, B. M., and Luther, G. W.: Simultaneous determination of soluble manganese(III), manganese(II) and total manganese in natural (pore)waters, Talanta, 84, 374–381, https://doi.org/10.1016/j.talanta.2011.01.025, 2011.

Madison, A. S., Tebo, B. M., Mucci, A., Sundby, B., and Luther, G. W.: Abundant porewater Mn (III) is a major component of the sedimentary redox system, science, 341, 875–878, 2013.

750 Meybeck, M.: Global chemical weathering of surficial rocks estimated from river dissolved loads, Am. J. Sci., 287, 401–428, 1987.

Meybeck, M.: Global occurrence of major elements in rivers, Treatise Geochem., 5, 605, 2003.

Meybeck, M., Cauwet, G., Dessery, S., Somville, M., Gouleau, D., and Billen, G.: Nutrients (organic C, P, N, Si) in the eutrophic River Loire (France) and its estuary, Estuar. Coast. Shelf Sci., 27, 595–624,
755 https://doi.org/10.1016/0272-7714(88)90071-6, 1988.

Middelburg, J. J., Soetaert, K., and Hagens, M.: Ocean Alkalinity, Buffering and Biogeochemical Processes, Rev. Geophys., 58, e2019RG000681, https://doi.org/10.1029/2019RG000681, 2020.

Millero, F. J.: ThermodynamicsOfficer, C. B.: Discussion of the carbon dioxide systembehaviour of nonconservative dissolved constituents in the oceans, Geochim. Cosmochim. Acta, 59, 661–677estuaries,

Estuar. Coast. Mar. Sci., 9, 91–94, https://doi.org/10.1016/~~0016-7037(94)00354-O, 1995~~0302-3524(79)90009-4, 1979.

Oldham, V. E., Jones, M. R., Tebo, B. M., and Luther, G. W.: Oxidative and reductive processes contributing to manganese cycling at oxic-anoxic interfaces, Mar. Chem., 195, 122–128, https://doi.org/10.1016/j.marchem.2017.06.002, 2017a.

Oldham, V. E., Miller, M. T., Jensen, L. T., and Luther, G. W.: Revisiting Mn and Fe removal in humic rich estuaries, Geochim. Cosmochim. Acta, 209, 267–283, https://doi.org/10.1016/j.gca.2017.04.001, 2017b.

Poulton, S. W. and Raiswell, R.: The low-temperature geochemical cycle of iron: from continental fluxes to marine sediment deposition, Am. J. Sci., 302, 774–805, 2002.

Raaphorst, W. V. and Malschaert, J. F. P.: Ammonium adsorption in superficial North Sea sediments, Cont. Shelf Res., 16, 1415–1435, https://doi.org/10.1016/0278-4343(95)00081-X, 1996.

Rassmann, J., Eitel, E. M., Lansard, B., Cathalot, C., Brandily, C., Taillefert, M., and Rabouille, C.: Benthic alkalinity and dissolved inorganic carbon fluxes in the Rhône River prodelta generated by decoupled aerobic and anaerobic processes, Biogeosciences, 17, 13–33, https://doi.org/10.5194/bg-17-13-2020, 2020.

Raven, J. A., Wollenweber, B., and Handley, L. L.: A comparison of ammonium and nitrate as nitrogen sources for photolithotrophs, New Phytol., 121, 19–32, https://doi.org/10.1111/j.1469-8137.1992.tb01088.x, 1992.

Rickard, D. and Luther, G. W.: Chemistry of Iron Sulfides, Chem. Rev., 107, 514–562, https://doi.org/10.1021/cr0503658, 2007.

Rudnick, R. L. and Gao, S.: Composition of the continental crust, Treatise Geochem., 3, 1–64, 2003.

~~Shen, C., Testa, J. M., Li, M., Cai, W. J., Waldbusser, G. G., Ni, W., Kemp, W. M., Cornwell, J., Chen, B., Brodeur, J., and Su, J.: Controls on Carbonate System Dynamics in a Coastal Plain Estuary: A Modeling Study, J. Geophys. Res. Biogeosciences, 124, 61–78, https://doi.org/10.1029/2018JG004802, 2019.~~

Sholkovitz, E. R., Shaw, T. J., and Schneider, D. L.: The geochemistry of rare earth elements in the seasonally anoxic water column and porewaters of Chesapeake Bay, Geochim. Cosmochim. Acta, 56, 3389–3402, 1992.

Sinex, S. A. and Helz, G. R.: Regional geochemistry of trace elements in Chesapeake Bay sediments, Environ. Geol., 3, 315–323, https://doi.org/10.1007/BF02473521, 1981.

Smith, S. V. and Mackenzie, F. T.: The Role of CaCO3 Reactions in the Contemporary Oceanic CO2 Cycle, Aquat. Geochem., 22, 153–175, https://doi.org/10.1007/s10498-015-9282-y, 2016.

Soetaert, K., Hofmann, A. F., Middelburg, J. J., Meysman, F. J. R., and Greenwood, J.: The effect of biogeochemical processes on pH, Mar. Chem., 105, 30–51, https://doi.org/10.1016/j.marchem.2006.12.012, 2007.

Stookey, L. L.: Ferrozine—a new spectrophotometric reagent for iron, Anal. Chem., 42, 779–781, 1970.

Su, J., Cai, W.-J., Brodeur, J., Chen, B., Hussain, N., Yao, Y., Ni, C., Testa, J. M., Li, M., Xie, X., Ni, W., Scaboo, K. M., Xu, Y., Cornwell, J., Gurbisz, C., Owens, M. S., Waldbusser, G. G., Dai, M., and Kemp, W. M.: Chesapeake Bay acidification buffered by spatially decoupled carbonate mineral cycling, Nat. Geosci., 13, 441–447, https://doi.org/10.1038/s41561-020-0584-3, 2020a.

Su, J., Cai, W., Brodeur, J., Hussain, N., Chen, B., Testa, J. M., Scaboo, K. M., Jaisi, D. P., Li, Q., Dai, M., and Cornwell, J.: Source partitioning of oxygen-consuming organic matter in the hypoxic zone of the Chesapeake Bay, Limnol. Oceanogr., 65, 1801–1817, https://doi.org/10.1002/lno.11419, 2020b.

Su, J., Cai, W., Testa, J. M., Brodeur, J. R., Chen, B., Scaboo, K. M., Li, M., Shen, C., Dolan, M., Xu, Y., Zhang, Y., and Hussain, N.: Supply-controlled calcium carbonate dissolution decouples the seasonal dissolved oxygen and pH minima in Chesapeake Bay, Limnol. Oceanogr., lno.11919, https://doi.org/10.1002/lno.11919, 2021.

Thamdrup, B.: New Pathways and Processes in the Global Nitrogen Cycle, Annu. Rev. Ecol. Evol. Syst., 43, 407–428, https://doi.org/10.1146/annurev-ecolsys-102710-145048, 2012.

Thamdrup, B. and Dalsgaard, T.: The fate of ammonium in anoxic manganese oxide-rich marine sediment, Geochim. Cosmochim. Acta, 64, 4157–4164, https://doi.org/10.1016/S0016-7037(00)00496-8, 2000.

Thibault de Chanvalon, A. and Luther, G. W.: Mn speciation at nanomolar concentrations with a porphyrin competitive ligand and UV–vis measurements, Talanta, 200, 15–21, https://doi.org/10.1016/j.talanta.2019.02.069, 2019.

Trouwborst, R. E., Clement, B. G., Tebo, B. M., Glazer, B. T., and Luther, G. W.: Soluble Mn(III) in Suboxic Zones, Science, 313, 1955–1957, https://doi.org/10.1126/science.1132876, 2006.

Urey, H. C.: On the Early Chemical History of the Earth and the Origin of Life, Proc. Natl. Acad. Sci., 38, 351–363, https://doi.org/10.1073/pnas.38.4.351, 1952.

Wolf-Gladrow, D. A., Zeebe, R. E., Klaas, C., Körtzinger, A., and Dickson, A. G.: Total alkalinity: The explicit conservative expression and its application to biogeochemical processes, Mar. Chem., 106, 287–300, https://doi.org/10.1016/j.marchem.2007.01.006, 2007.

Zeebe, R. E. and Wolf-Gladrow, D.: CO2 in seawater: equilibrium, kinetics, isotopes, Gulf Professional Publishing, 2001.

825   Zhang, Q., Brady, D. C., Boynton, W. R., and Ball, W. P.: Long-Term Trends of Nutrients and Sediment from the Nontidal Chesapeake Watershed: An Assessment of Progress by River and Season, JAWRA J. Am. Water Resour. Assoc., 51, 1534–1555, https://doi.org/10.1111/1752-1688.12327, 2015.